



# Effects of multi-stage rifting and metasomatism on HSE- $^{187}\text{Os}/^{188}\text{Os}$ systematics of the cratonic mantle beneath SW Greenland

Sonja Aulbach<sup>1</sup> · Jing Sun<sup>2</sup> · Sebastian Tappe<sup>3</sup> · Axel Gerdes<sup>1</sup>

Received: 7 October 2018 / Accepted: 21 January 2019 / Published online: 5 February 2019  
© Springer-Verlag GmbH Germany, part of Springer Nature 2019

## Abstract

We report highly siderophile element (HSE) abundances and Re–Os isotope compositions, obtained by isotope dilution inductively coupled plasma mass spectrometry, of olivine separates from a suite of multiply metasomatised peridotite xenoliths entrained in kimberlites from SW Greenland. Combined with petrographic and compositional observations on accessory base metal sulphides (BMS), the results reveal new insights into the chemical, physical and mineralogical effects of multi-stage rifting and associated melt percolation on the Archaean lithospheric mantle. Refertilised lherzolites are dominated by rare to frequent small (tens of  $\mu\text{m}$ ) BMS inclusions in olivine, whereas modally metasomatised phlogopite-bearing lherzolite and wehrlites have higher proportions of more Ni-rich BMS, including abundant large interstitial grains (hundreds of  $\mu\text{m}$ ). The olivine separates display depleted HSE systematics with Primitive Upper Mantle (PUM)-normalised Pd/Ir of 0.014–0.62, and have both depleted and enriched  $^{187}\text{Os}/^{188}\text{Os}$  (0.1139–0.2724) relative to chondrite that are not correlated with  $^{187}\text{Re}/^{188}\text{Os}$ . Four out of ten olivine separates retain similarly depleted Os corresponding to Re-depletion model ages of 2.1–1.8 Ga. They may reflect Palaeoproterozoic refertilisation (lherzolitisation) during Laurentia plate assembly, with re-introduction of clinopyroxene and Os-rich BMS into the originally refractory mantle lithosphere by asthenosphere-derived basaltic melts, followed by recrystallisation and occlusion in olivine. Unradiogenic Os is observed regardless of lithology, including from peridotites that contain abundant interstitial BMS. This reflects addition of Os-poor BMS ( $\ll 1$  ppm) during more recent wehrlitisation and phlogopite-introduction, and control of the Os isotopic signature by older Os-rich BMS that precipitated from the basaltic melt. Depletions in compatible HSE ( $< 0.5 \times \text{PUM}$  for Ru, Ir, Os) in all but one olivine separate reflect nugget effects (amount of depleted vs. metasomatic BMS inclusions) and/or loss due to sulphide dissolution into oxidising small-volume melts that invaded the lithosphere during recurrent rifting, the latter supported by similar depletions in published bulk peridotite data. Combined, these multiple metasomatic events destroyed all vestiges of Mesoarchaean or older inheritance in the olivine separates investigated here, and highlight that caution is needed when interpreting Proterozoic Os model ages in terms of Proterozoic lithosphere stabilisation.

**Keywords** Subcontinental lithosphere · Mantle metasomatism · Platinum-group elements · Highly siderophile elements · Base metal sulphides

---

Communicated by Chris Ballhaus.

---

**Electronic supplementary material** The online version of this article (<https://doi.org/10.1007/s00410-019-1549-7>) contains supplementary material, which is available to authorized users.

---

✉ Sonja Aulbach  
s.aulbach@em.uni-frankfurt.de

<sup>3</sup> Department of Geology, University of Johannesburg,  
P.O. Box 524, Auckland Park 2006, South Africa

<sup>1</sup> Institut für Geowissenschaften, Goethe Universität,  
Altenhöferallee 1, 60438 Frankfurt, Germany

<sup>2</sup> State Key Laboratory of Lithospheric Evolution, Institute  
of Geology and Geophysics, Chinese Academy of Sciences,  
Beijing 100029, China

## Introduction

The lithospheric mantle beneath cratonic Greenland (Fig. 1), part of the North Atlantic Craton, (hereafter: GNAC) and adjacent areas have experienced a multi-stage evolution. Multiple extension events, during the Mesoproterozoic (~ 1350–1140 Ma), Neoproterozoic (~ 610–550 Ma) and Mesozoic–Cenozoic, were accompanied by formation of low-volume melts in the sublithosphere, and ultimately resulted in the break-up of the NAC and opening of the Labrador Sea and Davis Strait (Tappe

et al. 2007, and references therein). Even older extensional events, at ca. 2.5 and 2.0 Ga, are indicated by the intrusion of dyke swarms (Nilsson et al. 2013). A part of the younger low-volume melts was subsequently immobilised through formation of metasomatic veins in the mantle lithosphere, and later reactivated due to continued thinning to generate a spectrum of ultramafic alkaline magmas. These include kimberlite, lamproite, lamprophyre and carbonatite, the mantle sources of which require variable proportions of phlogopite, carbonates and phlogopite–richterite–Ti oxide assemblages (Tappe et al. 2008, 2011), similar to those observed in some peridotite xenolith suites from the GNAC (Hanghøj et al. 2001; Aulbach et al. 2017). This tumultuous history has resulted in a chemically and mineralogically complex mantle lithosphere (Bernstein et al. 1998, 2006; Hanghøj et al. 2001; Bizzarro and Stevenson 2003; Hutchison et al. 2007; Hutchison and Heaman 2008; Wittig et al. 2008, 2010; Sand et al. 2009; van Acken et al. 2017). However, the nature and effects of these events within the cratonic mantle, which ultimately resulted in the loss of some 30–40 km of lithospheric mantle beneath the NAC on either side of the Labrador Sea (Tappe et al. 2007; Aulbach et al. 2017), remain incompletely understood.

Recent work has shown that the deep lithospheric root beneath the southwestern GNAC was affected by strong hydrous metasomatism that ultimately facilitated the formation of ultramafic melts within the diamond stability field and led to the development of a mid-lithospheric discontinuity, which may herald further decratonisation in the future (Aulbach et al. 2017; Aulbach 2019). To shed new light on the transformation of this complex cratonic lithosphere section, we use the Re–Os isotope system in combination with information from the HSE abundances of fresh olivine separates, rather than whole-rock peridotite, which frequently contains kimberlitic material. The Os isotopes provide model ages or at least constraints on long-term depletion and enrichment, as well as valuable context for the interpretation of the magmatic-metasomatic history of the peridotite samples. Given that sulphides and platinum-group minerals (PGM) are known to sequester highly siderophile elements (HSE), among them Re and Os with their embedded radioactive decay system (Shirey and Walker 1998), we also investigated the mineralogy and composition of BMS (Fe–Ni–Cu sulphides) occurring in these samples (no PGM were identified in this study). In contrast to the peridotite xenolith sample suite from SW-GNAC studied by Wittig et al. (2010), which is described as extremely serpentinised, the samples in the present study are exceptionally fresh. We here discuss (1) the observed and inferred HSE hosts in olivine separates and compare these to reported whole-rock data, (2) the effects of partial melting during lithosphere stabilisation and of re-introduction or removal of sulphides and other minerals during Proterozoic metasomatic events,

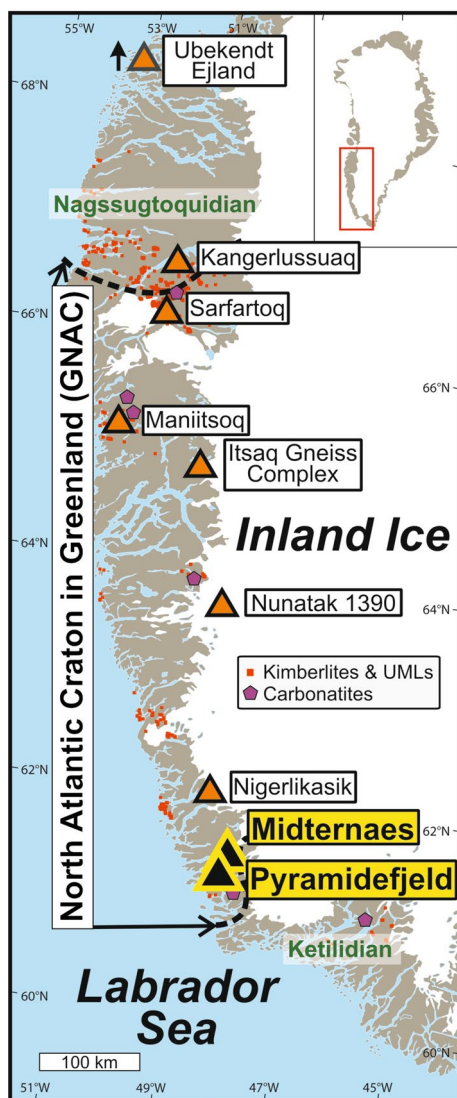


**Fig. 1** Map of southwestern Greenland with the outline of the North Atlantic Craton (NAC), mantle peridotite localities (this study and xenolith localities or outcrops reported in the literature) as well localities of kimberlites, ultramafic lamprophyres and carbonatites. Nagssugtoquidian and Ketilidian north and south of the craton boundary refer to Palaeoproterozoic orogenies

and (3) the effects of recurrent rifting and a major orogeny as well as more recent metasomatism on HSE systematics.

## Geology, samples and prior work

The GNAC was assembled during Neoproterozoic (ca. 2.7 Ga) convergence of cratonic nuclei (Griffin et al. 2004; Pearson and Wittig 2008, 2014; Windley and Garde 2009; Tappe et al. 2011a, b). The occurrence of ca. 2.5 and 2.0 Ga dike swarms attest to some early extensional events in the craton (Nilsson et al. 2013). Palaeoproterozoic collisions (1.9–1.7 Ga) and Laurentian plate assembly led to formation of the Nagssugtoqidian and Ketilidian orogens, which border the GNAC to the north and south (Hoffman 1989; Garde et al. 2002). Following these collisional craton-building and -shielding processes, several failed rifting episodes (1.4–1.2 Ga, 0.61–0.55 Ga, 0.14–0.10 Ga), followed by opening of the North Atlantic and craton breakup along the Labrador Sea margins, caused successive thinning of the cratonic lithospheric mantle (Tappe et al. 2007, 2011, 2012, 2017; Larsen et al. 2009). The attendant intrusion of kimberlites, ultramafic lamprophyres, and alkali basalts into the GNAC and bordering mobile belts exhumed mantle xenoliths and xenocrysts, including diamond (Bernstein et al. 1998, 2006, 2013; Wittig et al. 2008, 2010; Sand et al. 2009; Bizzarro and Stevenson 2003; Tappe et al. 2011a, b; Aulbach et al. 2017).

The shallow lithospheric mantle beneath some parts of Greenland (Wiedeman Fjord, central craton, and southern and northern margins of the western GNAC; Fig. 1) has experienced unusually high degrees of melt extraction (up to 40% at 2–3 GPa), resulting in strong depletion, as evidenced by high olivine modes (median 86 vol%), high forsterite contents in olivine (> 92) and low contents of incompatible elements, such as  $\text{Al}_2\text{O}_3$  (median 0.56 wt%), Pd (0.5 ppb) and Pt (1.1 ppb), and unradiogenic Os (< 0.11) (data in Hanghøj et al. 2001; Bennett et al. 2002; Wittig et al. 2008, 2010; Bernstein et al. 2006). Lithosphere formation in the Sarfartoq and Maniitsoq areas, near the northern GNAC margin and on the GNAC, respectively (Fig. 1), was dated to the Mesoproterozoic and Neoproterozoic, based on Re–Os and Pb–Pb isotopes of mantle xenoliths (and their constituents) entrained in 590–550 Ma and 160–150 Ma kimberlites and ultramafic lamprophyres, but Proterozoic metasomatic episodes were also identified (Wittig et al. 2010; Tappe et al. 2011a, b; van Acken et al. 2017). Indeed, a generally more fertile lithospheric mantle layer is found in the northern GNAC, where cpx introduction has clearly affected the composition of the primary assemblage in that silicates in lherzolites have lower Mg/Fe and Cr/Al than those in the refractory harzburgites and dunites (Sand et al. 2009). A

relatively high geothermal gradient determined for garnet peridotite xenoliths from the ca. 150 Ma Pyramidefjeld and Midternaes kimberlites in the SW-GNAC (corresponding to a surface heat flow of 42–44  $\text{mW/m}^2$ ; Nielsen et al. 2008), compared to that for mantle xenoliths from 590 to 550 Ma kimberlites and ultramafic lamprophyres in the NW-GNAC ( $\sim 38 \text{ mW/m}^2$ ; Sand et al. 2009), was ascribed to intervening heating and lithosphere thinning during incipient rifting of the NAC (Tappe et al. 2007, 2012, 2017; Larsen et al. 2009).

Samples in the present study were originally collected in 2007 during fieldwork by Louise Nielsen and stored at the Geological Survey of Denmark and Greenland—GEUS. They represent a subset of 42 fresh peridotite xenoliths from the Mesozoic (ca. 150 Ma) Pyramidefjeld and Midternaes kimberlite dyke and sill localities at the southwestern margin of the GNAC (Fig. 1) (Emeleus and Andrews 1975; Frei et al. 2008; Larsen et al. 2009). Based on the presence or absence of pyroxenes and phlogopite, samples were classified as lherzolites (olivine, opx, cpx), harzburgites (olivine, opx), dunites (olivine) and wehrlites (olivine, cpx) with and without phlogopite (prefix “phl-” denotes the presence of phlogopite) (Aulbach et al. 2017). Note that dunites in the suite have olivine with low Mg# (median 90.3 compared to lherzolite with Mg# 91.3), and are olivine-rich due to reaction with silica-undersaturated melt rather than to extreme depletion; the single dunite investigated in the present study is hereafter referred to as “reaction dunite” to highlight this origin (cf. Arndt et al. 2010). Accessory spinel occurs in most samples. Clinopyroxene and phlogopite in wehrlites are irregularly distributed, but are texturally equilibrated as indicated by  $120^\circ$  grain boundaries (Fig. 2; Online Appendix 1).

A detailed in-situ analytical campaign combined with petrographic investigation revealed the presence of two xenolith types with respect to mineralogy, metasomatic style and depth of residence in the cratonic lithosphere. The first group comprises lherzolites, harzburgites and dunites derived from  $\sim 100$ – $170$  km depth, which were metasomatised by hydrous silicate melt just prior to entrainment in the kimberlite. This was accompanied by garnet breakdown and an increase in  $\text{TiO}_2$ , MnO and  $\text{Na}_2\text{O}$  as well as a decrease in NiO and Mg#. The second group comprises phl-wehrlites and phl-peridotites showing evidence for recent pyroxene-breakdown, derived from  $\sim 90$ – $110$  km depth. They are suggested to have interacted with residual, more silica-undersaturated and potentially more oxidising melts that percolated upwards from deeper lithospheric levels. These xenoliths differ from the deeper lherzolites in having olivine with higher Ca/Al, but lower V contents, ascribed to a combination of intrinsically more oxidising mantle at lower pressure and oxidative metasomatism (Aulbach et al. 2017).

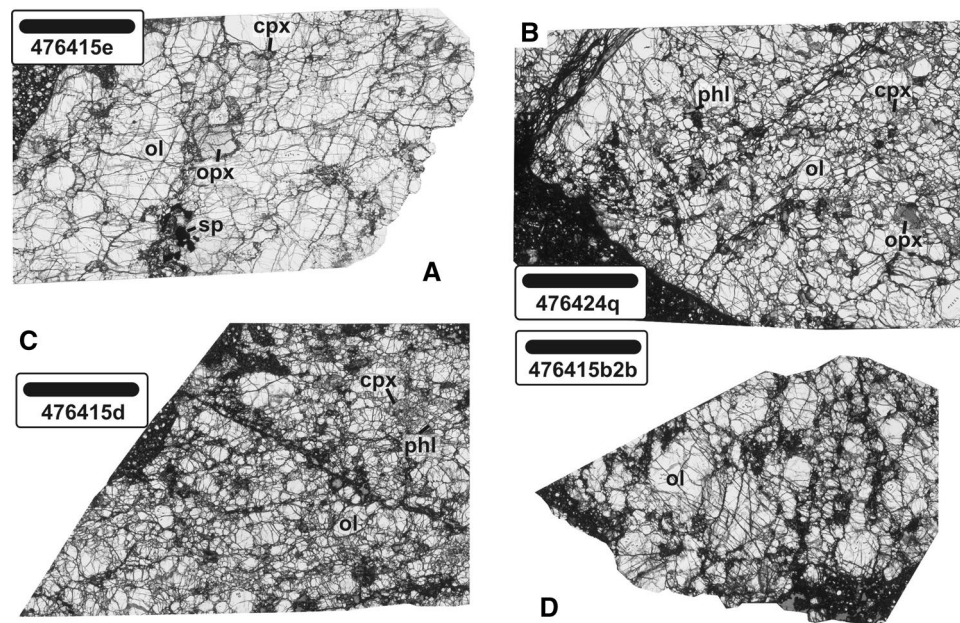


**Fig. 2** Representative thin section photographs (plane-polarised light) of peridotite xenoliths from southwestern Greenland, consisting of coarse-equant lherzolites (**a**), which grade into variably metasomatised medium- to coarse-grained phl-lherzolites (**b**), opx-free wehrlites (**c**) and reaction dunites (**d**) showing tabular textures. Scale bar is 1 cm. Orthopyroxene clasts appear cloudy due to oriented exsolutions of cpx. Of note, phlogopite (beige colour) and secondary cpx

(minty green colour) in the metasomatised samples are texturally equilibrated. Microcrystalline alteration patches, presumably replaced former pyroxene, have mossy green colour. Most samples show veins and melt pools connected to the kimberlite matrix. *Ol* olivine, *opx* orthopyroxene, *cpx* clinopyroxene, *phl* phlogopite, *kimb* kimberlite, *sp* spinel

## Sample preparation and analytical techniques

All work was carried out at the Institute of Geosciences, Goethe-University Frankfurt. Following the methods outlined in Aulbach et al. (2012), sulphide minerals in thick section were analysed for major and minor elements (Fe, Co, Ni, Cu, S) by electron microprobe, using a JEOL JX 8900 instrument operated at an acceleration voltage of 20 kV, beam current of 30 nA and nominal beam diameter of 1  $\mu\text{m}$ . Pure metals (Ni, Co, Cu) and troilite were used as calibration standards, and a pyrite secondary standard was analysed as an unknown to monitor data quality (Online Appendix 2). Because some O, which was not independently determined, may be present in the BMS, analyses with totals down to 97.5 wt% are accepted. Silicon was monitored in order to detect overlapping analyses with neighbouring silicate grains (i.e., mixed compositions). In addition, back-scattered electron (BSE) images were taken using the same instrument, or a scanning electron microprobe, in order to study internal grain features (Online Appendix 3).

Trace-element abundances in exsolution-free areas of sulphide assemblages (see “Sulphide petrography” and Online Appendix 3) were determined with a Thermo

Finnigan Element-2 inductively-coupled plasma mass spectrometry (ICPMS) instrument linked to a RESOLUTION (Resonetics) 193 nm ArF Excimer Laser (CompexPro 102, Coherent), following the approach detailed in Aulbach et al. (2012). Briefly, the measurement conditions included spot sizes for standards and samples of 43  $\mu\text{m}$  (20  $\mu\text{m}$  for small grains) and use of a 50% attenuator to avoid high fluence on the samples and elemental fractionation associated with sample melting (Wohlgemuth-Ueberwasser et al. 2007). Alteration, abundant cracks and exsolution of inferred former mss to low-temperature assemblages, combined with the minimum spot size requirement for useful measurement statistics, imply that only few grains in three peridotite samples, plus a pyrite grain in the kimberlite matrix, were amenable to in situ analysis by laser ablation. Sulphur concentrations as determined by EPMA were used as internal standard. Synthetic reference materials LaFlamme-Po727 (pyrrhotite; Godel and Barnes 2008), PGE\_Ni7b (Ni sulphide; Wohlgemuth-Ueberwasser et al. 2007) and MASS-1 (pressed Zn sulphide powder; Wilson et al. 2002) were used for sensitivity calibration, and each standard was analysed three times to mitigate the effects of possible heterogeneity. Data were reduced with the Glitter software (Griffin et al. 2008). Accuracy and precision can

be tested only for HSE contained within both standards (LaFlamme-Po727 and PGE\_Ni7b) and show that abundances in the latter reproduce within 20% of accepted values, except for Pt (23%).

Considering the generally high Ni and Co concentrations in the measured BMS and the abundances of the metal isotopes involved, argide interferences ( $^{61}\text{Ni}^{40}\text{Ar}$  on  $^{101}\text{Ru}$  and  $^{59}\text{Co}$  on  $^{99}\text{Ru}$ ) preclude accurate determination of Ru concentrations. The same applies to analyses of Cu-rich sulphides where Cu argides ( $^{63}\text{Cu}^{40}\text{Ar}$ ,  $^{65}\text{Cu}^{40}\text{Ar}$ ) interfere with  $^{103}\text{Rh}$  and  $^{105}\text{Pd}$ , while  $^{106}\text{Pd}$  is affected by an interference from  $^{66}\text{Zn}^{40}\text{Ar}$ . Thus, the average apparent Ru and Rh concentration for nominally Rh, Ru- and Pd-free standard MASS-1 is 0.4 and 35 ppm, respectively, while the apparent Pd concentration derived from  $^{105}\text{Pd}$  and  $^{106}\text{Pd}$  is 62 and 9 ppm, respectively. This corresponds to Cu and Zn argide production rates of  $\sim 0.03\%$  and  $0.004\%$ , respectively. Strong positive correlations are consequently observed between Ni and Ru and between Cu and Rh and  $^{105}\text{Pd}$ . We therefore do not report abundances for Ru and Rh, and report Pd abundances only for BMS with  $< 600$  ppm Cu, where the correlation between Cu and Pd breaks down. For the remaining samples, Pd abundances results derived from  $^{105}\text{Pd}$  and  $^{106}\text{Pd}$  are similar. Results for BMS and standards, including measurement statistics, detection limits and standard deviations for multiple spots, where available, are given in Online Appendix 4.

Acquisition of bulk rock HSE abundances by isotope dilution ICPMS and of Re–Os isotopes by isotope dilution multicollector (MC) ICPMS largely follows the method outlined in Aulbach et al. (2014). Briefly, approximately 1 g of clear (i.e. unaltered, not cloudy) olivine, in part containing opaque inclusions, was separated under the binocular, and ultrasonicated and rinsed twice in Milli-Q  $\text{H}_2\text{O}$ . Mixed  $^{101}\text{Ru}$ – $^{106}\text{Pd}$ – $^{191}\text{Ir}$ – $^{198}\text{Pt}$  and  $^{185}\text{Re}$ – $^{190}\text{Os}$  spikes were added to the dried and powdered olivine separates, followed by addition of aqua regia and sealing for digestion (6–10 h) in a high-pressure asher (HPA-S from Anton Paar) at a temperature of 300 °C and pressure of 100 bar. Osmium was subsequently extracted into chloroform and back-extracted into HBr, dried down and measured by MC ICPMS, employing a Thermo Finnigan Neptune instrument in static collection mode using Faraday cups. Sample solutions were introduced via microconcentric nebuliser (Elemental Scientific Inc.), combined with a Cinnabar mini-cyclonic spray chamber (Glass Expansion).

The residue was dried down, re-dissolved and processed through 10 ml cation exchange resin for chromatographic separation of HSE from the matrix. The HSE were measured on a sector-field ICPMS instrument (Thermo Finnigan Element-2) with sample introduction in mixed Ar– $\text{N}_2$  gas via an Aridus spray chamber. Contrary to the previously described routine (Aulbach et al. 2014), Re was measured

by MC ICPMS in a setup identical to Os to avoid the Re build-up plaguing analyses with the Aridus spray chamber. The significantly lower sensitivity of the glass spray chamber was compensated by the greatly reduced Re memory compared to the Aridus and resultant lower detection limits, and led to improved reproducibility of Re abundances in the reference material. Concentrations were calculated from ratios corrected for argide, oxide, and isobaric interferences as well as mass bias using isotope dilution equations. Full procedural blanks ( $n=5$ ; Ru =  $0.0087 \pm 0.0065$  ppb; Pd =  $0.011 \pm 0.011$  ppb, Ir =  $0.0022 \pm 0.0021$  ppb, Pt =  $0.0032 \pm 0.0007$  ppb, Re =  $0.019 \pm 0.009$  ppb, Os =  $0.0109 \pm 0.0045$  ppb) contributed on average from  $< 1\%$  for Ir to 5% for Re to the sample signal (Online Appendix 5). Samples were run back to back over the course of  $\sim 1$ – $1.5$  h with ca. 5 min measurement followed by 5 min of wash-out. Normalisation to the in-house Os plasma standard, the isotopic composition of which was independently determined using thermal ionisation mass spectrometry (Aulbach et al. 2014), resulted in small corrections, where duplicates ( $n=5$ ) of 1 ppb solutions on the 2 days of sample measurements yielded  $0.14228 \pm 0.00098$  and  $0.14307 \pm 0.00098$ , respectively. The long-term reproducibility of a 10 ppb solution of this in-house standard for 13 analytical campaigns between January 2012 and February 2015 is  $0.1433 \pm 0.0015 2\sigma$ , compared to the TIMS-derived value of  $0.143240 \pm 0.000047$ . The peridotite reference material UB-N (Meisel et al. 2003; Meisel and Moser 2004) was processed along with samples for quality control ( $n=5$ ) and both HSE concentrations (Ru =  $6.60 \pm 0.37$  ppb, Pd =  $5.90 \pm 0.16$  ppb, Ir =  $3.27 \pm 0.21$  ppb, Pt =  $7.37 \pm 0.31$  ppb, Re =  $0.184 \pm 0.04$  ppb, Os =  $3.71 \pm 0.39$  ppb) and  $^{187}\text{Os}/^{188}\text{Os}$  ( $0.1282 \pm 0.0004$ ) compare well with published data (Online Appendix 5).

## Results

### Sulphide petrography

BMS are most abundant in wehrlite 476407i, whereas with one exception, lherzolites are BMS-poor. BMS crystal sizes, shapes and mineralogy vary widely between and within lithologies, as summarised in Table 1: (1) Small (tens of  $\mu\text{m}$ ) ovoid to subhedral grains included in olivine, but now mostly connected to the matrix via cracks (i.e., “pseudo-inclusions”), in part with smaller “satellite grains” occurring in the vicinity; (2) large (hundreds of  $\mu\text{m}$ ) irregular grains, in part with corroded grain boundaries, occurring interstitially, often with trails of small sulphide flakes occurring within nearby veins, but also within associated olivine grains; (3) agglomerations of multiple intermediate-sized ( $\sim 50$ – $100 \mu\text{m}$ ) anhedral grains in association

**Table 1** Rock types, base metal sulphide habits and assemblages in peridotite xenoliths from southwestern cratonic Greenland

Sample	Rock type	Incl <sup>a</sup>	Int <sup>b</sup>	Agg <sup>c</sup>	Assemblages
476407i	Wehrlite	+	+++	++	pn + po ± cpy
476414a	Phl-wehrlite	++	++	++	pn + cpy, Ni-rich “mss”, pn
476415b	Lherzolite	+	+	+	po, py
476415b2a	Lherzolite	+	–	–	pn ± cpy
476415b2b	Dunite	+	–	–	pn + po, pn + “mss”
476415d	Phl-wehrlite	++	–	–	“mss” ± pn
476415e	Lherzolite	+	–	–	pn + cpy
476415h1	Lherzolite	+	–	–	Ni-rich “mss”, “mss”+pn
476424b1	Lherzolite	+	+	–	Ni-rich “mss”+cpy ± pn, po + pn
476424q	Phl-lherzolite	+	++	+++	pn ± cpy

Cpy chalcopyrite, “mss” BMS with monosulphide solid solution-like composition, pn pentlandite, po pyrrhotite, py pyrite

– Absent, + present, ++ abundant. +++ very abundant

<sup>a</sup>Inclusions: small (10 s μm) ovoid to subhedral grains included in olivine, but now mostly connected to the matrix via cracks (i.e., “pseudo-inclusions”)

<sup>b</sup>Interstitial large (100 s μm) irregular grains, in part with corroded grain boundaries

<sup>c</sup>Agglomerations of multiple intermediate-sized (~50–100 μm) anhedral grains in association with veins or altered patches

with veins or altered patches; (4) small sulphide flakes associated with cryptocrystalline veins or grain boundary components or decrepitation trails of larger grains (cf. van Acken et al. 2017). Within grains, exsolutions of elongate irregular laths or blocks of Ni-rich and Ni-poor BMS are ubiquitous, with Cu-rich BMS occasionally observed at the rims. While refertilised lherzolites are dominated by rare to frequent small ( $\leq$  tens of μm) BMS inclusions in olivine (type 1), modally metasomatised phl-lherzolite and two of three wehrlites additionally contain abundant large (hundreds of μm) interstitial grains (type 2 and 3).

## Sulphide mineralogy and element concentrations

Figure 3 shows BMS compositions in the Fe–(Ni + Co) S (at%) quadrilateral with respect to stoichiometric sulphides and solid solutions. Iron-rich BMS with Me/S (Me = metal = Fe, Co, Ni, Cu)  $\sim$  1 are assigned to pyrrhotite, including BMS with up to 6.3 at% Ni. BMS with higher S contents ( $\geq$  53 at% vs.  $<$  51 at% for other BMS) and lower Me/S (0.86 to 0.89) are compositionally similar to monosulphide solid solution (mss) (6.1–12.9 at% Ni), although they probably represent low-temperature re-equilibration

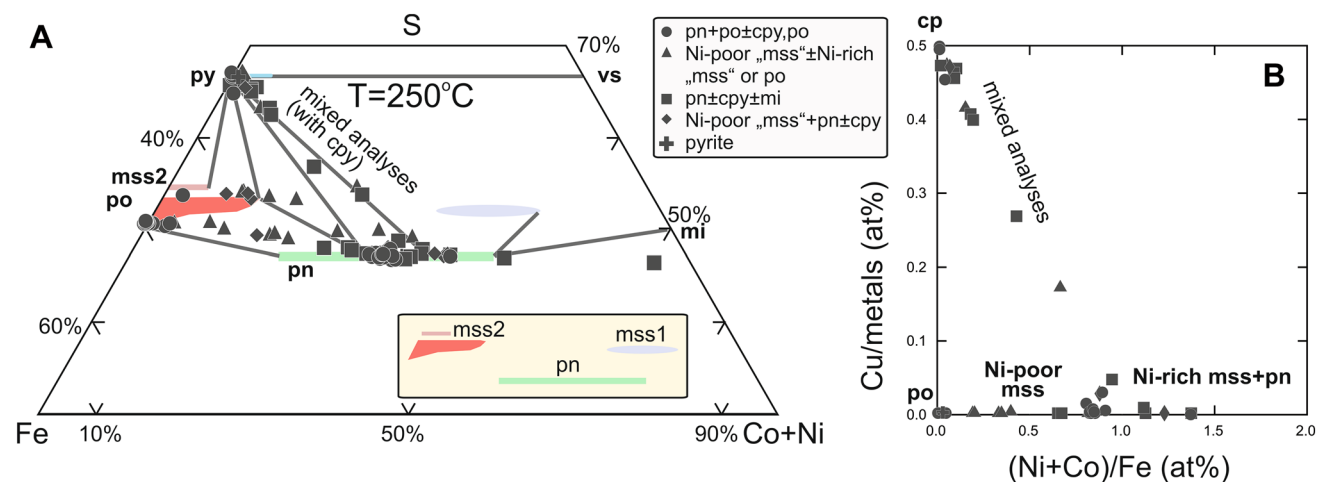


**Fig. 3** Average sulphide mineral compositions (not reconstructed bulk compositions of exsolved grains) **a** in the Fe–(Ni + Co) S (at%) quadrilateral, with phase relations in the system Fe–Ni–S and 250 °C and atmospheric pressure (after Craig 1973; Lorand and Grégoire 2006) and **b** in a diagram of atomic (Ni + Co)/Fe vs. Cu/metals (met-

als = Fe + Co + Ni + Cu). Almost all pentlandite (pn), mss-like BMS (“mss”), chalcopyrite (cpy) and pyrrhotite (po) analyses are for exsolved areas within discrete BMS grains inferred to represent former high-temperature mss. Pyrite (py) and millerite (mi) have been detected in two samples, vaesite (vs) is not present

products; they will be referred to here as “mss” for simplicity. Pentlandites differ from the latter in having higher Me/S ( $\geq 1.06$ ) and higher Ni (14.3–35.6 at%). A few BMS have intermediate Ni (11.2–22.4 at%) and Me/S (1.02–1.04), which are designated as Ni-rich “mss”. For small grains and for thin chalcopyrite rims or narrow exsolution features, ‘clean’ analyses were not always possible. Multiple spot analyses of some BMS yield variable proportions of Ni and Fe, which may reflect overlaps between neighbouring exsolved patches or incomplete exsolution. Where partial alteration has occurred, it has obliterated predominantly Fe-rich parts of the exsolved assemblage, leading to a predominance of pentlandite or Ni-rich “mss” and chalcopyrite analyses. In all sulphide minerals except in pentlandite, Co contents correlate with Ni contents and both are anti-correlated with S. In pentlandite, Co contents vary strongly (factor 2: 0.40–0.84 wt%) at relatively constant Ni (23.1–32.0 wt%) (e.g., 476407i).

BMS in wehrlites, reaction dunite and phl-lherzolite are characterised by assemblages of pentlandite, pyrrhotite  $\pm$  chalcopyrite, or pentlandite  $\pm$  chalcopyrite, or just Ni-rich “mss” (Table 1). Pyrrhotite and chalcopyrite contain minor amounts of Ni (0.1–2.4 at% and 0.1–1 at%, respectively) and both have Me/S  $\sim 1$  (Table 2). Partially altered pentlandite inclusions in phl-wehrlite 476414a are less Ni-rich (19–23 at%) than those occurring interstitially (27 at%). In contrast, inclusions in phl-wehrlite 476415d consist of “mss” (7.6–12.9 at% Ni) with low Me/S (0.86–0.89). BMS in lherzolites consist of pentlandite or Ni-rich “mss”  $\pm$  “mss” and chalcopyrite, and in one case (476415b) they are exclusively S- and Fe-rich, with two pyrrhotite pseudo-inclusions (Co + Ni  $< 0.2$  at% and Me/S = 0.97) and pyrite in an interstitial agglomeration.

Unfortunately, only few intact patches in few BMS grains (pentlandite and pyrrhotite in two grains each in wehrlite 476407i, Ni-rich “mss” in lherzolite 476424b, pentlandite in three grains in phl-wehrlite 476424q) lent themselves to in situ trace-element analysis. This precludes the recognition of variations among different lithologies. In addition, bulk BMS could not be reconstructed because not all minerals in the low-temperature assemblage could be analysed. With these caveats in mind, some systematics may be discerned between minerals making up the low-temperature assemblages of former high-temperature mss. The single Ni-rich “mss” measured in the lherzolite has the highest Re (0.30 ppm), but the lowest As contents (0.076 ppm), and Sb below detection ( $< 0.018$  ppm). Pyrrhotite tends to be poorer in trace elements than the pentlandites, having mostly lower Zn, As, Mo, Ag, Sn, Os and Ir contents, and Sb below detection ( $< 0.03$  ppm), but Pt contents are similar and Re and Cr contents tend to be higher (Table 3). BMS in the wehrlites and lherzolite from the highly metasomatised lithospheric layer in the SW-GNAC investigated here have median Os

(0.017 ppm), Ir (0.009 ppm), Pt (0.028 ppm) and Pd contents (0.22 ppm) that are lower than those in two types of BMS identified in a harzburgite from the northern GNAC margin, where the type with high abundances of compatible Ir-group platinum-group elements (IPGE: Ru, Os, Ir) contains 52, 46, 2.2 and 1.7 ppm, respectively, of Os, Ir, Pt and Pd, and the IPGE-poor type contains 0.20, 0.17, 2.0 and 2.2 ppm, respectively (van Acken et al. 2017). Concentrations of the HSE are also generally lower than in orogenic (König et al. 2014) and abyssal peridotites (Luguet et al. 2001) (Fig. 4). Median PUM-normalised Pt/Ir (PUM of Becker et al. 2006; denoted with subscript PUM) is 4.7 and does not vary systematically between pentlandite and “mss”, whereas Re/Os<sub>PUM</sub> is higher in “mss” (51 and 510) than in pentlandite (4.0–15.7). Selenium contents (median 35 ppm) are at the low end of those reported for orogenic peridotites, while Te contents (median 8.5 ppm) are at the high end, resulting in low Se/Te (median 4.2 for all sulphide minerals) relative to most orogenic peridotites. Compared to peridotitic BMS, kimberlitic pyrite is trace-element poor, having low Cr, the lowest Zn, Ag, Sn and HSE contents, but the highest As contents (10 ppm). Selenium contents are similar, but Te contents are an order of magnitude lower, resulting in much higher Se/Te (56) than in peridotite sulphide minerals ( $\leq 8.2$ ).

### Olivine HSE concentrations, Os isotopes and model ages

The compatible IPGE and even more so Pt-group PGE (PPGE: Pd, Pt) concentrations in olivine separates vary by one to two orders of magnitude (Ru from 0.18 to 4.38 ppb, Os from 0.12 to 3.38 ppb, Ir from 0.17 to 2.16 ppb and Pd from 0.02 to 0.95 ppb, Pt from 0.03 to 1.14 ppb), with no significant difference between olivine from lherzolites and phl-wehrlites (Table 3; Fig. 5). Rhenium concentrations vary from 0.07 to 0.51 ppb, with one outlying value at 2.3 ppb for 476407i, which is the most BMS-rich peridotite. All olivine separates show depletions in the incompatible PPGE relative to the compatible IPGE (Pd/Ir<sub>PUM</sub> from 0.014 to 0.62), but there is some complexity: Two olivine separates (476415e, 476415b2b) show decreasing PUM-normalised IPGE abundances (Os  $>$  Ir  $>$  Ru) while the olivine fraction from lherzolite 76415h1 is enriched in Pd, but also has the least fractionated Pd/Pt<sub>PUM</sub> and an overall relatively flat HSE pattern (Fig. 6).

The  $^{187}\text{Os}/^{188}\text{Os}$  values of the olivine separates range from 0.1139 to 0.2724, again without a clear separation according to lithological type. Unradiogenic  $^{187}\text{Os}/^{188}\text{Os}$  (0.1137–0.1226) is observed in olivine separates from lherzolites, wehrlites and the single reaction dunite (Fig. 5c). These Os isotopic compositions translate into Re-depletion model ages ( $T_{\text{RD}}$ ; Shirey and Walker 1998) from 2.13 to

**Table 2** Textural setting, grain shape and mineralogy and major element composition of representative base metal sulphides in peridotite xenoliths from southwestern cratonic Greenland

Mineral	Si (wt%)	Fe (wt%)	Co (wt%)	Ni (wt%)	Cu (wt%)	S (wt%)	Total	Me/S	Ni/(Ni + Fe)
<i>Wehrlite 476407i S1—interstitial—large ovoid corroded—pn + po</i>									
pn (10)	2.86	34.70	0.74	30.29	<0.12	32.87	98.7	1.12	0.45
po (4)	0.02	61.40	0.10	0.22	<0.12	36.53	98.3	0.97	0.00
<i>Wehrlite 476407i S5—pseudoinclusion—large subhedral corroded—pn + po</i>									
pn (5)	0.03	35.20	0.77	29.95	0.18	32.66	98.8	1.14	0.45
po (4)	0.02	61.47	0.10	<0.11	<0.12	36.20	97.8	0.98	0.00
<i>Wehrlite 476407i S6—pseudoinclusion—medium euhedral—pn + po</i>									
pn (5)	0.05	36.18	0.84	28.88	<0.12	32.89	98.9	1.13	0.43
po (4)	0.02	61.36	0.11	0.24	<0.12	36.52	98.3	0.97	0.00
<i>Wehrlite 476407i S7—pseudoinclusion—medium subhedral—pn + po</i>									
pn (4)	0.03	35.05	0.48	29.27	1.04	32.78	98.6	1.13	0.44
po (4)	0.02	61.13	0.10	<0.11	<0.12	36.31	97.7	0.97	0.00
<i>Wehrlite 476407i S8—interstitial—large angular embayed—pn + po</i>									
pn (4)	0.03	34.78	0.52	30.68	<0.12	32.78	98.8	1.13	0.46
po (7)	0.03	61.23	0.11	0.40	<0.12	36.31	98.1	0.98	0.01
<i>Wehrlite 476407i S9—medium roundish corroded—pn + po</i>									
pn (4)	0.03	36.37	0.71	28.59	<0.12	33.14	98.9	1.11	0.43
po (4)	0.02	60.58	0.13	0.99	<0.12	36.38	98.1	0.97	0.02
<i>Wehrlite 476407i S11—interstitial—large ovoid corroded—pn + po + cpy</i>									
cpy (2)	0.02	29.60	0.07	0.23	33.91	34.16	98.0	1.00	0.01
pn (4)	0.04	35.21	0.72	29.74	0.23	32.63	98.6	1.13	0.45
po (6)	0.02	60.74	0.11	0.57	<0.12	36.19	97.7	0.97	0.01
<i>Wehrlite 476407i S15—interstitial—large irregular corroded/agglomeration—pn + po + cpy</i>									
cpy (1)	0.04	29.58	<0.09	0.31	33.98	34.52	98.5	0.99	0.01
pn (2)	0.05	33.49	0.62	31.98	<0.12	32.52	98.7	1.14	0.48
po (2)	0.07	58.32	0.15	3.20	<0.12	36.18	97.9	0.98	0.05
<i>Wehrlite 476407i S17—interstitial—large irregular corroded/agglomeration—pn + po + cpy</i>									
cpy (2)	0.02	29.51	<0.09	<0.11	33.87	34.51	98.0	0.99	0.00
pn (2)	0.02	34.66	0.45	30.26	0.49	32.84	98.7	1.12	0.45
po (1)	0.02	61.26	0.10	0.09	<0.12	36.25	97.8	0.97	0.00
<i>Wehrlite 476407i S19—interstitial—large angular embayed—pn + po + cpy</i>									
cpy (4)	0.06	31.62	0.09	1.26	31.08	34.65	98.8	1.00	0.04
pn (4)	0.05	34.63	0.69	30.29	0.25	33.05	99.0	1.12	0.45
po (2)	0.03	61.35	0.11	0.08	<0.12	36.55	98.1	0.97	0.00
<i>Phlogopite-wehrlite 476414a S1—interstitial—large irregular aggregate—pn + cpy</i>									
cpy (1)	0.02	28.81	<0.09	3.14	31.87	34.47	98.4	1.00	0.09
pn (1)	0.02	30.08	0.48	34.83	0.76	32.92	99.1	1.12	0.52
<i>Phlogopite-wehrlite 476414a S2—included—small euhedral remnant in altered grain—Ni-rich “mss”</i>									
Ni-rich “mss” (4)	0.05	38.77	0.37	23.79	<0.12	34.56	97.5	1.03	0.37
<i>Phlogopite-wehrlite 476414a S6—interstitial—medium irregular/agglomeration—pn</i>									
pn (1)	0.22	29.20	0.28	34.22	0.14	32.63	96.7	1.09	0.53
<i>Phlogopite-wehrlite 476414a S8—included—small euhedral remnant in altered grain—Ni-rich “mss”</i>									
Ni-rich “mss” (3)	0.03	34.36	0.55	24.73	<0.12	38.93	98.6	0.86	0.41
<i>Lherzolite 476415b S1—pseudoinclusion—medium subhedral corroded—po</i>									
po (5)	0.03	61.49	0.12	<0.11	<0.12	36.53	98.3	0.97	0.00
<i>Lherzolite 476415b S2—pseudoinclusion—small subhedral po</i>									
po (2)	0.02	61.54	0.10	<0.11	<0.12	36.66	98.3	0.97	0.00
<i>Lherzolite 476415b S3—interstitial—small irregular/agglomeration—py</i>									
py (1)	0.43	43.29	0.26	1.12	0.14	50.90	96.1	0.50	0.02
<i>Lherzolite 476415b2a S1—pseudoinclusion—medium roundish partially altered—pn + cpy</i>									
pn (4)	0.03	38.50	0.67	25.74	0.15	33.77	98.9	1.08	0.39
~cpy (1)	0.53	30.74	0.34	13.41	18.38	33.06	96.5	1.04	0.29

**Table 2** (continued)

Mineral	Si (wt%)	Fe (wt%)	Co (wt%)	Ni (wt%)	Cu (wt%)	S (wt%)	Total	Me/S	Ni/(Ni + Fe)
<i>Lherzolite 476415b2a S3—pseudoinclusion—medium roundish partially altered with small included satellite grain—pn</i>									
Pn (6)	0.06	45.06	0.45	18.42	0.25	34.16	98.4	1.06	0.28
<i>Reaction dunite 476415b2b S2—included—small euhedral—pn + po</i>									
po (1)	0.05	55.89	0.10	2.81	<0.12	39.02	97.9	0.86	0.05
pn (1)	0.04	26.93	0.70	38.12	<0.12	32.59	98.4	1.12	0.57
<i>Reaction dunite 476415b2b S3—included—small euhedral—pn + "mss"</i>									
"mss" (2)	0.04	47.87	0.30	11.43	<0.12	38.69	98.4	0.88	0.19
pn (3)	0.03	27.77	0.52	37.75	<0.12	32.83	98.9	1.12	0.56
<i>Phlogopite wehrlite 476415d S1—included—small roundish—"mss"</i>									
"mss" (3)	0.03	42.57	0.47	17.01	<0.12	38.15	98.2	0.89	0.28
<i>Phlogopite wehrlite 476415d S4—included—small subhedral—pn + "mss"</i>									
"mss" (2)	0.03	45.77	0.34	13.63	<0.12	38.48	98.3	0.88	0.22
pn (1)	0.03	30.53	0.53	33.17	<0.12	34.18	98.5	1.05	0.51
<i>Phlogopite wehrlite 476415d S9—included—small subhedral—pn + "mss"</i>									
pn (1)	0.05	27.35	0.59	38.09	<0.12	33.11	99.2	1.11	0.57
"mss" (2)	0.04	48.18	0.40	10.53	<0.12	39.30	98.5	0.86	0.17
<i>Lherzolite 476415e S1—pseudoinclusion—medium subhedral—pn + cpy</i>									
pn (4)	0.03	37.92	0.54	26.34	0.14	33.27	98.2	1.10	0.40
cpy (2)	0.04	30.82	<0.09	0.56	32.08	34.46	98.0	0.99	0.02
<i>Lherzolite 476415h1 S1—included—small euhedral—Ni-rich "mss" + "mss"</i>									
Ni-rich "mss" (1)	0.06	34.13	0.36	28.86	0.08	34.83	98.3	1.02	0.45
"mss" (1)	0.07	48.27	0.21	9.94	<0.12	38.58	97.2	0.86	0.16
<i>Lherzolite 476415h1 S2—included—small roundish—pn + "mss"</i>									
pn (2)	0.06	28.26	0.33	36.18	0.14	32.61	97.6	1.11	0.55
"mss" (1)	0.10	49.03	0.19	7.95	<0.12	38.00	95.3	0.86	0.13
<i>Lherzolite 476415h1 S3—included—small euhedral—cpy (+ Ni-rich sulphide, unclean analysis)</i>									
cpy (1)	0.07	29.76	<0.09	1.54	32.00	34.72	98.2	0.98	0.05
<i>Lherzolite 476424b1 S1—pseudoinclusion (large vein)—large subhedral—Ni-rich "mss" + cpy</i>									
cpy (1)	0.16	30.72	0.16	4.86	28.67	34.30	98.9	1.02	0.13
Ni-rich "mss" (2)	0.05	47.26	0.40	16.03	<0.12	34.74	98.6	1.04	0.24
<i>Lherzolite 476424b1 S2—pseudoinclusion—large subhedral partially altered—pn + Ni-rich "mss" + cpy</i>									
cpy (1)	0.04	29.81	<0.09	2.08	32.29	34.55	98.8	1.00	0.06
Ni-rich "mss" (3)	0.34	47.76	0.31	14.21	<0.12	34.44	97.1	1.03	0.22
pn (1)	0.12	33.12	0.55	30.05	2.12	33.00	99.0	1.12	0.46
<i>Lherzolite 476424b1 S4—interstitial medium irregular—pn + po</i>									
pn (2)	0.07	32.75	0.47	30.26	2.23	32.67	98.4	1.12	0.47
po (2)	0.03	61.13	0.10	0.16	<0.12	36.34	97.9	0.97	0.00
<i>Phlogopite wehrlite 476424q S1—interstitial—large elongate irregular—pn + cpy</i>									
cpy (1)	0.08	29.44	<0.09	2.65	31.53	34.50	98.3	0.99	0.08
pn (3)	0.05	31.28	0.26	30.80	3.45	33.25	99.1	1.10	0.48
<i>Phlogopite wehrlite 476424q S2—pseudoinclusion—large irregular embayed—pn</i>									
pn (7)	0.03	27.11	0.40	38.86	0.14	33.17	99.7	1.12	0.58
<i>Phlogopite wehrlite 476424q S3—interstitial—large irregular embayed—pn + cpy</i>									
cpy (4)	0.02	29.85	<0.09	2.82	31.18	34.70	98.7	0.99	0.08
pn (4)	0.03	31.61	0.58	33.84	<0.12	32.82	98.9	1.13	0.50

See Online Appendix 3 for backscatter electron images of the sulphides described here

Me/S metal (Fe,Co,Ni,Cu)/sulphur; Me/S and Ni/(Ni + Fe) in at%

Small 10 s of  $\mu\text{m}$ , medium ~ 50–100  $\mu\text{m}$ , large 100–100 s of  $\mu\text{m}$

Cpy chalcopyrite, "mss" BMS with monosulphide solid solution-like composition, pn pentlandite, po pyrrhotite, py pyrite; number in parentheses is number of averaged analyses

**Table 3** Trace-element composition (ppm; in situ measurements) and measurement statistics of sulphides in kimberlite and in peridotite xenoliths from SW Greenland

	476407i s1 (1) Pyrrhotite	476407i s4 (4) Pentlandite	476407i s16 (1) Pentlandite	476407i s16 (3) Pyrrhotite	476424q s2 (1) Pentlandite	476424b s1 (1) Ni-rich "mss"	476424q s3 (2) Pentlandite	476424q s5 (1) Pentlandite	424q kimb (2) Pyrite
<i>Against Mass1</i>									
Cr53	200.0	2.3	70.7	116.7	0.9	13.4	26.5	45.1	1.4
Co59	442	1313	3230	202	853	1399	1288	2443	102
Cu65	62.2	1423.3	195.7	28.8	14046.5	626.0	360.0	216.3	163.4
Zn66	1.6	26.6	106.1	4.2	63.5	3.4	1.7	7.1	1.2
As75	<0.126	3.4	0.8	0.4	7.9	0.2	2.4	3.5	10.0
Se77	33	67.8	39	35.2	32	50	35	30	35.0
Mo95	1.450	na	3.350	1.970	1.338	2.360	9.880	202.900	11.710
Ag107	0.544	20.943	10.210	1.259	1.680	0.979	2.060	2.670	0.099
Sn118	<dl	na	<0.044	0.028	0.408	<dl	0.024	0.233	0.024
Sb121	<dl	0.243	0.050	<dl	0.356	<dl	0.111	0.655	9.245
Te125	6.9	8.24	11.0	7.66	8.2	8.8	24.4	15.8	0.63
<i>Against Po727</i>									
Pd105 <sup>a</sup>	0.056	na	0.574	0.074	na	na	0.150	0.252	0.059
Pd106 <sup>a</sup>	<dl	0.632	0.302	0.042	0.103	0.459	0.142	0.347	<dl
Os190	<dl	0.018	<dl	0.008	<dl	0.007	0.531	0.106	0.001
Ir193	0.003	0.012	0.003	<dl	<dl	0.007	0.485	0.066	<dl
Pt195	0.028	0.026	0.259	<dl	<dl	0.305	0.022	<dl	0.006
Au197	0.036	0.039	<0.021	0.023	0.148	0.083	0.163	0.047	0.018
<i>Against PGENi7b</i>									
Ni60	36,119	224,445	258,906	27,854	239,717	128,124	200,905	205,836	68
Re185	0.146	0.024	0.190	0.165	0.045	0.304	0.182	0.130	0.005

Number in parentheses is number of measurements averaged for sulphide grains with > 1 spot measured; measurement statistics and results for reference materials reported in Online Appendix 4

<sup>a</sup>Ru and Rh abundances for samples are not reported due to Ni and Cu argide interferences; Pd abundances derived from mass 105 are reported for samples with < 600 ppm Cu; see text for details

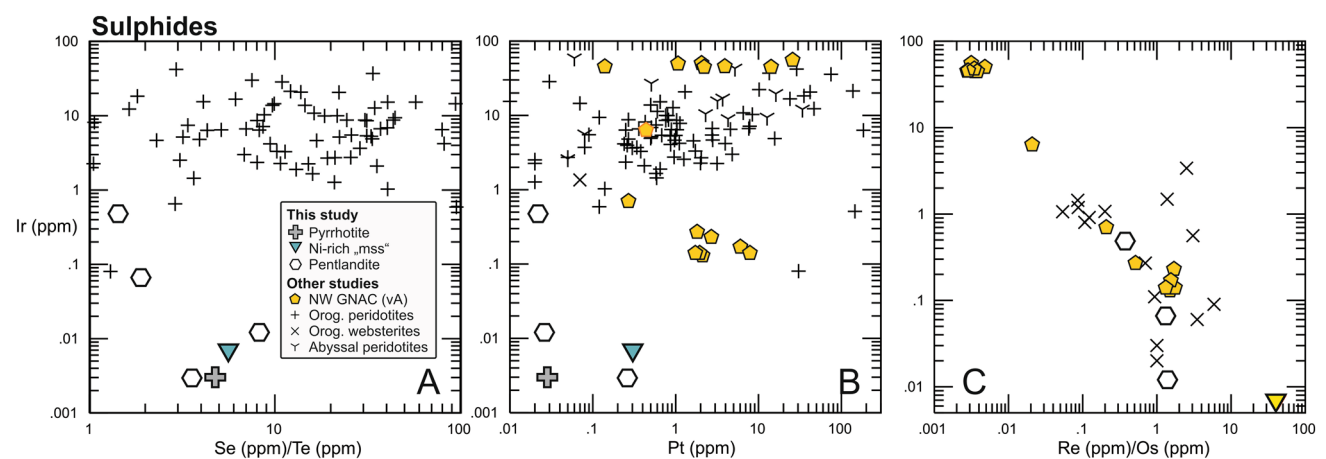


**Fig. 4** Trace element abundances and ratios in low-temperature sulphide minerals forming part of composite BMS grains; Pd concentrations are averages from those obtained from <sup>105</sup>Pd and <sup>106</sup>Pd reported in Table 3. Shown for comparison are BMS in a harzburgite from the

NW-GNAC margin ("vA"; van Acken et al. 2017), in orogenic peridotites ("Orog.", König et al. 2014) and websterites (van Acken et al. 2010), and in abyssal peridotites (Luguet et al. 2001)

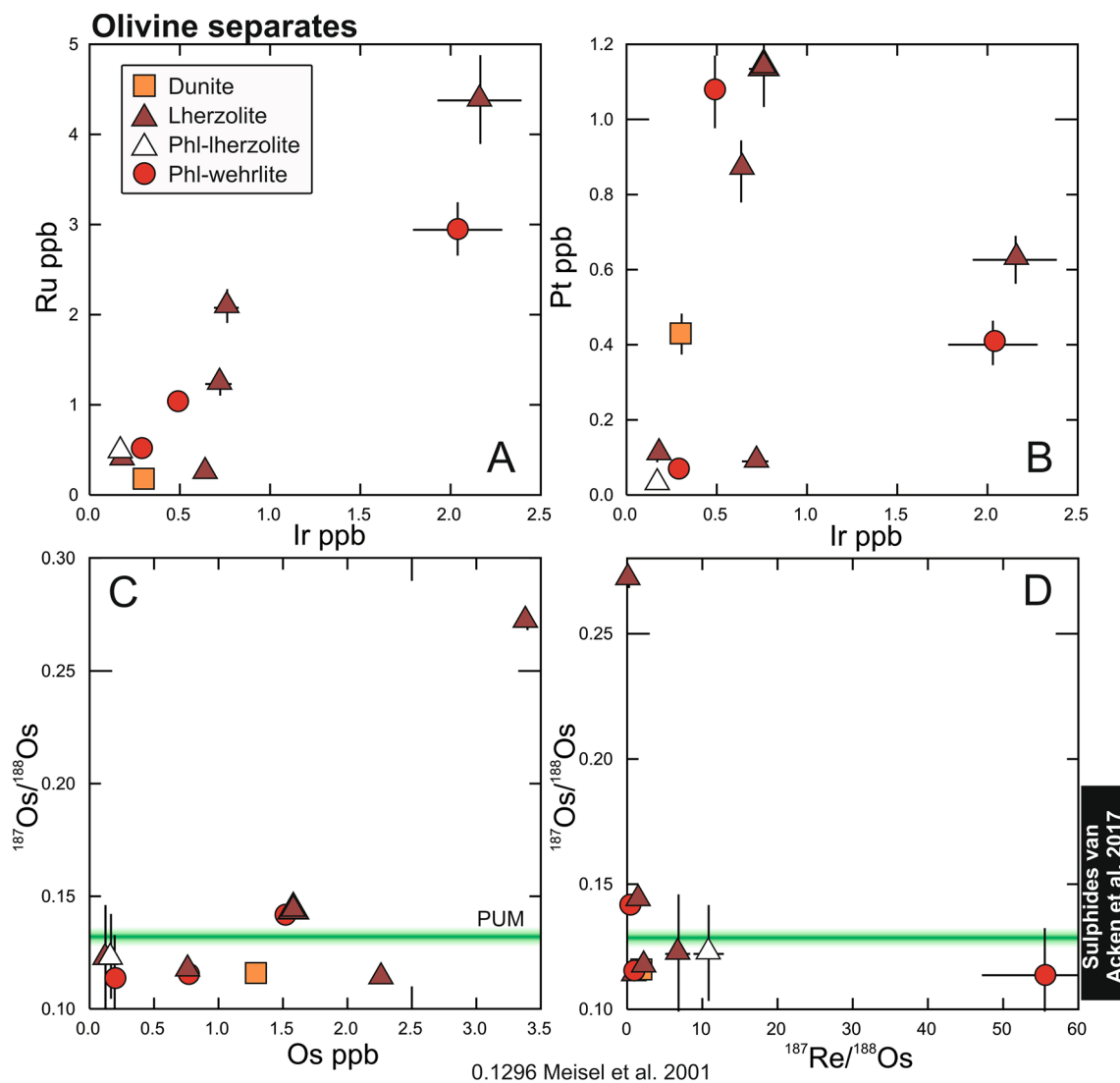


**Fig. 5** HSE systematics (a, b),  $^{187}\text{Os}/^{188}\text{Os}$  in olivine separates as a function of Os concentration (c), and Re–Os isochron diagram (d); range of  $^{187}\text{Os}/^{188}\text{Os}$  for individual sulphide grains in a mantle xenolith from off northwestern cratonic Greenland (Kangerlussuaq;

van Acken et al. 2017) shown as a black bar on right. In C. and D.  $^{187}\text{Os}/^{188}\text{Os}$  of the Primitive Upper Mantle (PUM:  $0.1296 \pm 0.0008$ ; Meisel et al. 2001) is shown for comparison. Error bars are  $2\sigma$

0.95 Ga (Table 4). The olivine separate with the highest  $^{187}\text{Os}/^{188}\text{Os}$  (lherzolite 476415e), which contains only few BMS grains on thin section scale, is characterised by the highest Os and second highest Pd contents, but intermediate Ru and Ir, and very low Pt abundances (Table 4). In the Re–Os isochron diagram (Fig. 5d), the olivine separates show no correlation, with unsupported radiogenic Os ( $\gamma_{\text{Os}}$ , as defined in the Footnote to Table 4 = 112) observed for lherzolite 476415e with low  $^{187}\text{Re}/^{188}\text{Os}$  (0.10), and unradiogenic Os ( $\gamma_{\text{Os}} = -11.2$ ; Table 4) observed for wehrlite 476407i, which has the highest  $^{187}\text{Re}/^{188}\text{Os}$  (56).

## Discussion

### Preservation of depleted $^{187}\text{Os}/^{188}\text{Os}$ in olivine from strongly metasomatised mantle

Peridotite xenoliths from cratonic and circumcratonic Greenland suggest the presence of an exceptionally refractory mantle lithosphere that features olivine-rich assemblages with correspondingly low bulk rock CaO and  $\text{Al}_2\text{O}_3$  contents (e.g. Bernstein et al. 1998, 2006). Despite the presence of Eoarchaean crust in the GNAC,

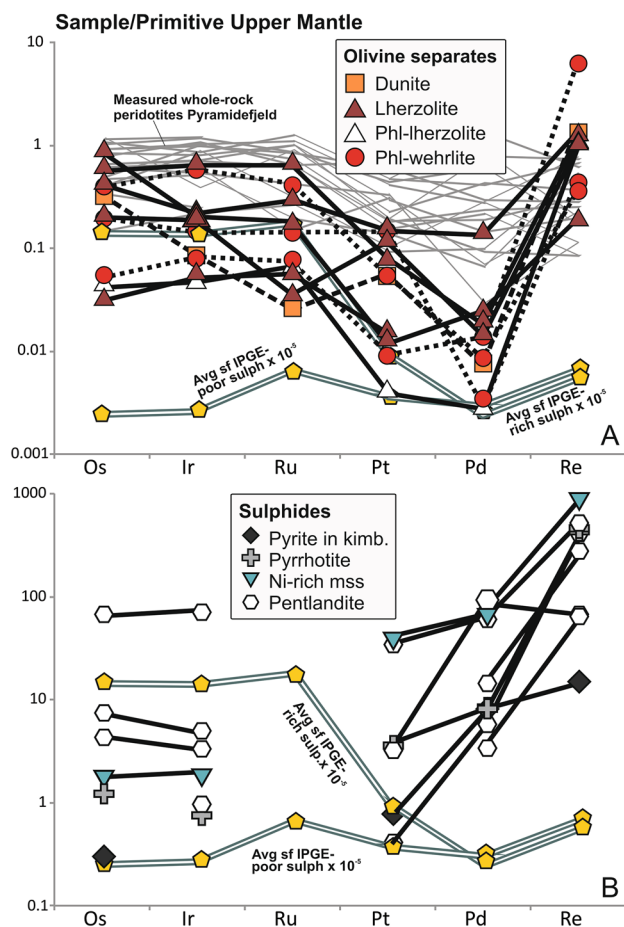


**Fig. 6** Primitive Upper Mantle (PUM)-normalised HSE abundances for **a** olivine separates; note that in contrast to lithophile elements, element order is conventionally from compatible (Os, Ir, Ru) to increasingly incompatible (Pt, Pd, Re). Shown for comparison are patterns for measured bulk rock peridotites from Pyramidefeld (Wittig et al. 2010) and averaged compositions of two BMS (sf) types identified by van Acken et al. (2017) in a mantle xenolith from off northwestern cratonic Greenland (Kangerlussuaq), of which one is IPGE-rich and the other is IPGE-poor; note that concentrations of the latter were divided by 100,000 for better comparability with olivine patterns. **b** Low-temperature pentlandite, Ni-rich “mss” and pyrrhotite, inferred to have exsolved from a high-temperature mss, as well as kimberlitic (“kimb.”) pyrite; concentrations of the two BMS types are here divided by 100. PUM from Becker et al. (2006)

which preserves  $^{146}\text{Sm}$ – $^{142}\text{Nd}$  and  $^{190}\text{Pt}$ – $^{186}\text{Os}$  isotope evidence for a Hadean mantle fractionation event (Bennett et al. 2007; Coggon et al. 2013), similarly old ages have not been obtained from deeply derived mantle xenoliths in the same area. Instead, lithospheric mantle stabilisation beneath Greenland has been dated to the Meso-/Neoproterozoic (Wittig et al. 2010; van Acken et al. 2017). A memory of these events is not preserved in the peridotites under investigation here, which all yield post-Archaeozoic Re-depletion ages (Table 4). As in previous Re–Os isotope studies on Greenland peridotite xenoliths, there is

no correspondence between Re/Os and  $^{187}\text{Os}/^{188}\text{Os}$  that would permit an isochron approach to dating events in the lithospheric mantle (Wittig et al. 2010) (Fig. 5d). The unusually strong disturbance of this otherwise robust isotope system is likely due to multiple rifting episodes affecting the GNAC, that were all accompanied by migration of small-volume carbonate-rich melts derived from the underlying convecting mantle (Tappe et al. 2007, 2012, 2017), combined with its setting at the southern craton margin where it was affected by the Palaeoproterozoic Ketilidian orogeny (Fig. 1).

A metasomatic event around 2 Ga was previously proposed based on a distinct mode of Re-depletion ages for peridotite samples from Pyramidefeld and also at the northern GNAC margin (Wittig et al. 2010; van Acken et al. 2017). The samples analysed by Wittig et al. (2010) are described as dominantly pyroxene- and garnet-poor to -free dunites and harzburgites, with minor phlogopite restricted to kimberlite-related contamination. Similarly, the sample investigated by van Acken et al. (2017) contains phlogopite only in the grain boundary component and in secondary serpentinite veins. In our study, a rather consistent Palaeoproterozoic isotopic signature is preserved in four out of ten peridotites ( $T_{\text{RD}}$  of ca. 2.1–1.8 Ga), including two phl-wehrlites, which were affected by strong refertilisation and/or more recent hydrous metasomatism and which contain olivine with relatively low Mg# (89) typical of fertile mantle. This highlights the—at least local—robustness of ancient Os isotopic signatures during multiple subsequent rifting events.

A detailed in situ investigation of pentlandite-rich BMS in a single harzburgite xenolith from just off the northern GNAC margin (Kangerlussuaq) revealed extreme Os isotopic heterogeneity ( $^{187}\text{Os}/^{188}\text{Os}$  of 0.1037–0.1981; van Acken et al. 2017). Given that the corresponding bulk rock has a  $^{187}\text{Os}/^{188}\text{Os}$  of 0.1129, similar to olivine separates with Palaeoproterozoic ages in this study, the interpretation of this whole-rock age as geologically meaningful is a concern. However, Os concentrations in these BMS also vary by more than three orders of magnitude (van Acken et al. 2017), and although there is some scatter in the data, the least radiogenic Os is observed in BMS with high concentrations and vice versa. In that study, whole-rock  $^{187}\text{Os}/^{188}\text{Os}$  is controlled by five grains with median Os concentrations of 113 ppm, of which four grains have a very restricted range in  $^{187}\text{Os}/^{188}\text{Os}$  (0.1118–0.1135) and one has  $^{187}\text{Os}/^{188}\text{Os}$  of 0.1192. In contrast, the remaining twelve grains have a median Os concentration of 2.5 ppm and  $^{187}\text{Os}/^{188}\text{Os}$  of 0.1260. Although all samples at all scales (bulk rock to individual BMS grains) likely carry an unknown amount of the metasomatic component (van Acken et al. 2017), the  $^{187}\text{Os}/^{188}\text{Os}$  of olivine separates investigated here may be controlled by Os-rich BMS with a relatively coherent and thus geologically meaningful

**Table 4** PGE-Re contents and Re–Os isotope systematics of olivine separates from xenoliths from SW Greenland

Sample	Rock type	Ru ppb	2 $\sigma^a$	2SE% <sup>b</sup>	Pd ppb	2 $\sigma^a$	2SE% <sup>b</sup>	Ir ppb	2 $\sigma^a$	2SE% <sup>b</sup>	Pt ppb	2 $\sigma^a$	2SE% <sup>b</sup>
476407i	wehr	0.52	0.06	1.0	0.10	0.08	7.1	0.29	0.03	0.8	0.07	0.02	1.6
476414a	phl wehr	2.95	0.29	0.8	0.06	0.03	4.3	2.04	0.25	0.8	0.41	0.06	1.3
476415b	lherz	4.38	0.50	0.8	0.13	0.02	1.6	2.16	0.23	0.8	0.63	0.06	1.0
476415b2a	lherz	0.40	0.05	1.2	na	na	na	0.18	0.02	1.0	0.11	0.02	1.4
476415b2b	dun	0.18	0.03	1.7	0.05	0.03	3.9	0.30	0.05	1.3	0.43	0.05	1.2
476415d	phl wehr	1.04	0.11	0.9	0.02	0.03	20.2	0.49	0.04	0.6	1.08	0.10	0.9
476415e	lherz	1.24	0.13	0.9	0.17	0.04	2.0	0.72	0.07	0.8	0.09	0.02	1.4
476415h1	lherz	2.09	0.18	0.7	0.95	0.13	1.2	0.76	0.07	0.8	1.14	0.10	0.9
476424b1	lherz	0.25	0.03	1.3	0.10	0.06	5.1	0.64	0.04	0.6	0.87	0.08	0.9
476424q	phl lherz	0.48	0.06	1.2	0.02	0.01	4.4	0.17	0.02	0.9	0.03	0.01	1.8
Sample		Re ppb	2 $\sigma^a$	2SE% <sup>b</sup>	Os ppb	2 $\sigma^a$	2SE% <sup>b</sup>	<sup>187</sup> Re/ <sup>188</sup> Os	2 $\sigma^a$	<sup>187</sup> Os/ <sup>188</sup> Os <sub>N</sub> <sup>c</sup>	2 $\sigma^a$	$\gamma_{Os}^d$	$T_{RD}^e$
476407i	wehr	2.28	0.31	1.0	0.20	0.01	0.0	55.62	8.25	0.1139	0.0187	−11.2	2131
476414a	phl wehr	0.13	0.03	1.4	1.52	0.01	0.0	0.43	0.11	0.1420	0.0027	10.7	na
476415b	lherz	0.41	0.08	1.3	2.26	0.01	0.0	0.88	0.16	0.1139	0.0019	−11.2	2126
476415b2a	lherz	0.16	0.04	1.3	0.12	0.00	0.0	6.72	1.58	0.1226	0.0232	−4.5	960
476415b2b	dun	0.51	0.12	1.7	1.29	0.01	0.0	1.90	0.45	0.1161	0.0031	−9.5	1839
476415d	phl wehr	0.16	0.04	1.4	0.77	0.00	0.0	0.97	0.23	0.1163	0.0034	−9.3	1804
476415e	lherz	0.07	0.02	1.4	3.38	0.01	0.0	0.10	0.03	0.2724	0.0036	112.3	na
476415h1	lherz	0.48	0.13	1.9	1.58	0.01	0.0	1.46	0.40	0.1448	0.0024	12.8	na
476424b1	lherz	0.35	0.06	1.2	0.76	0.01	0.0	2.20	0.40	0.1181	0.0041	−8.0	1566
476424q	phl lherz	0.36	0.06	1.2	0.16	0.00	0.0	10.79	2.00	0.1226	0.0190	−4.4	951

<sup>a</sup>Standard deviations reflecting instrumental uncertainties, weighing errors (0.0001 g for sample and spike weights) and blank uncertainties plus error magnification due to non-ideal sample-spike ratios

<sup>b</sup>Standard errors in % reflecting instrumental uncertainties

<sup>c</sup>Normalised to the OsFRA in-house plasma standard value (Aulbach et al. 2014)

<sup>d</sup>Denotes % deviation from ordinary chondrite with an Os isotope ratio of 0.1283 (Horan et al. 2003). This value is intermediate between carbonaceous and enstatite chondrites and represents a compromise that gives conservative results, but is not meant to imply that enstatite chondrites are Earth's main building blocks (Aulbach et al. 2016)

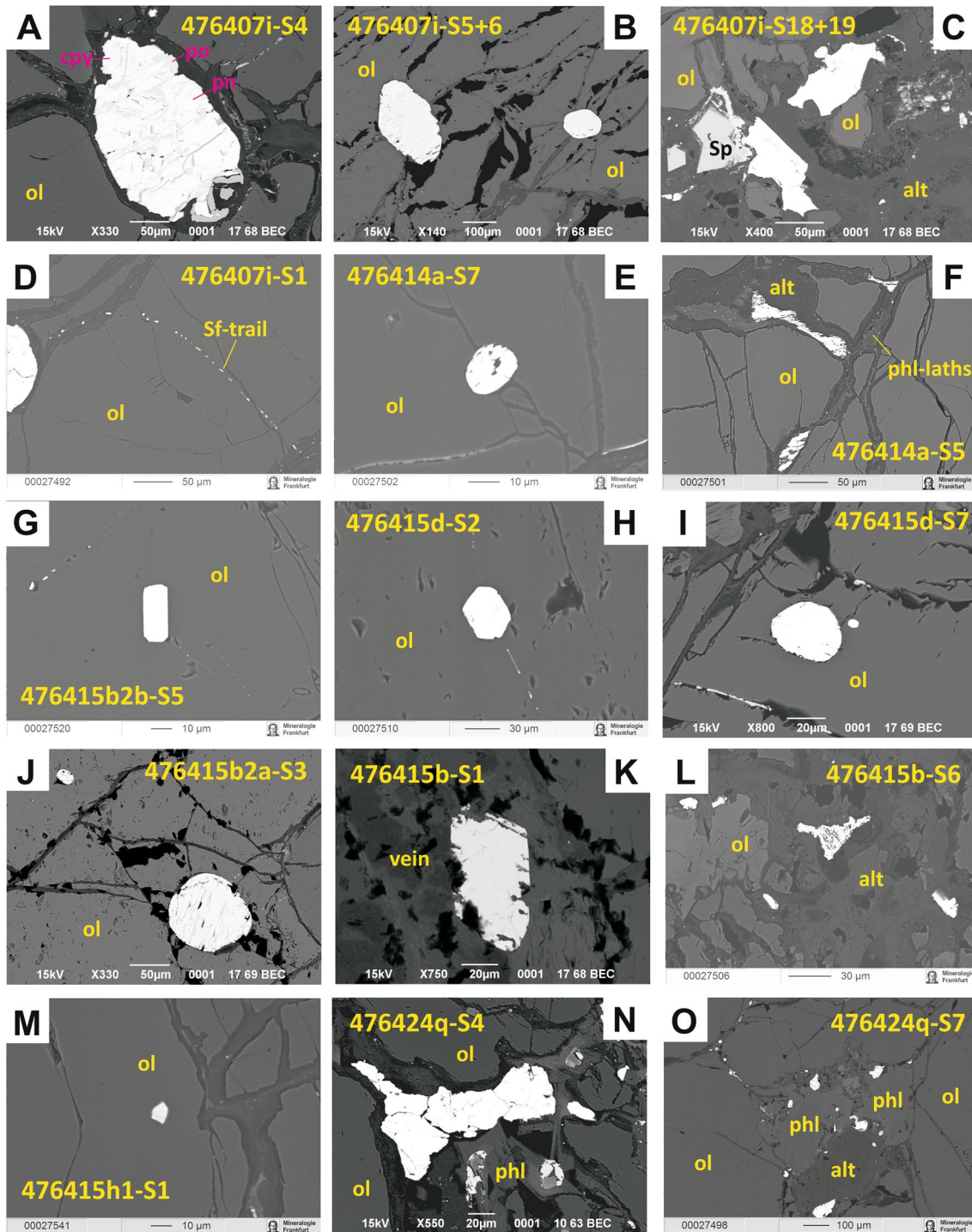
<sup>e</sup>Re depletion age (Shirey and Walker 1998), assuming that all Re is extracted during partial melting of PUM resulting in zero Os isotope evolution, hence only calculated for samples with unradiogenic Os, using values of Meisel et al. (2001)

isotopic signature. Consistent with this, sulphide minerals in abundant BMS in modally metasomatised phl-lherzolite and wehrilite in this study are Os-poor ( $\ll 1$  ppm; Table 3) and, even if they were radiogenic, have little leverage on the bulk rock <sup>187</sup>Os/<sup>188</sup>Os.

Although it would be tempting to ascribe preservation of the ca. 2 Ga Os isotopic signature in olivine separates to the protection of BMS of the type occurring in reaction dunite 476415b2b (Fig. 7, Online Appendix 3) by their silicate host, unradiogenic Os is also observed in olivine containing pseudo-inclusions which are mineralogically and chemically indistinguishable from matrix BMS (wehrilite 476407i). This reinforces recent findings that there is no correspondence between textural or mineralogical sulphide types and HSE patterns or Os isotopic signatures (Wainwright et al. 2015; van Acken et al. 2017).

### Sulphur re-introduction into the cratonic mantle during Proterozoic refertilisation

The GNAC mantle was originally strongly depleted by extraction of up to 40% of partial melt (Bernstein et al. 2007; Wittig et al. 2008)—implying a loss of the original sulphide and cpx content (Keays 1995; Walter 2014). The fact that most peridotite xenoliths investigated here contain variable, in cases copious amounts of BMS, as well as cpx, implies that they must have been metasomatically re-introduced, as previously noted by Wittig et al. (2010). This phenomenon is not restricted to the GNAC, as Proterozoic re-introduction of S into the initially strongly depleted Palaeoarchean cratonic mantle of the Kaapvaal craton in southern Africa is indicated by Re–Os dating of sulphide inclusions in diamond indicates (Aulbach et al. 2009). Indeed, the pentlandite-rich and rather constant composition of BMS in a peridotite xenolith from



Greenland was suggested to reflect a metasomatic origin, by melt/rock reaction associated with precipitation of chromite, cpx and BMS at the expense of garnet and opx (van Acken et al. 2017).

A narrow range of  $^{187}\text{Os}/^{188}\text{Os}$  (0.1139–0.1161) is observed in both refertilised lherzolites and metasomatised phl-wehrlites, encompassing two mineralogically and compositionally distinct mantle intervals at ~100

and 140 km, respectively. Refertilisation involved conversion of refractory dunite and harzburgite to lherzolite, yet depleted Os isotopic signature occurs in olivine with low Mg# (down to 89), which is typical of primitive rather than depleted mantle (e.g. Walter 2014). Re-depletion ages up to 2.80 Ga have been reported for olivine separates from Pyramidefeld (though 19 of 23  $T_{\text{RD}}$  are post-Archaean; Wittig et al. 2010). Similar ages have been obtained for crustal

**Fig. 7** Backscattered-electron images illustrating textural settings, shapes, grain sizes and internal structures of BMS in peridotite xenoliths from southwestern Greenland. **a–d** BMS in wehrlite 476407i: **a, b** show several large (up to several 100  $\mu\text{m}$ ) grains with elongate roundish to subhedral shapes, corroded boundaries and internal elongate or blebby exsolution of Fe- and Ni-rich BMS, with minor Cu-rich BMS. In **b**, a medium-sized grain with subhedral grain boundaries is also observed. **c** Large angular grain, consisting of a blocky assemblage of Fe- and Ni-rich BMS. **d** Trail of micron-sized grains associated with a large BMS grain. **e, f** BMS in phl-wehrlite 476414a: **e** is representative of a population of small BMS (pseudo-) inclusions (tens of  $\mu\text{m}$ ) dominated by roundish to subhedral shapes, while **f** is representative of a population consisting of abundant Ni-rich BMS grains (tens of  $\mu\text{m}$ ), intergrown with or overgrown by phlogopite laths and featuring minor exsolutions into Ni-rich and Ni-poor areas. **g** Representative of a population of small subhedral to roundish grains included in olivine in reaction dunite 476415b2b. **h, i** BMS in phl-wehrlite 476415d, which is dominated by numerous isolated small (tens of  $\mu\text{m}$ ) subhedral to euhedral BMS inclusions in olivine, in one case with a Ni-rich, minute (few  $\mu\text{m}$ ) grain next to it (in panel **i**). **j** Two roundish BMS grains ( $\sim 20$  and  $120 \mu\text{m}$ ) in close proximity (within  $\sim 200 \mu\text{m}$ ) in lherzolite 476415b2a. **k, l** BMS in lherzolite 476415b: **k** shows Fe-rich subhedral BMS grain with corroded grain boundary occurring in a fracture within olivine and **l** a concentration of Ni-rich anhedral grains in an altered patch. **m** One of three small ( $\sim 10 \mu\text{m}$ ) subhedral BMS inclusions in olivine in lherzolite 476415h1. **n, o** BMS in phl-lherzolite 476424q: **n** shows aggregates of large Ni-rich grains with interlocking to curvilinear grain boundaries and several smaller irregular grains occurring close-by, while **o** shows concentrations of exsolved, partially altered grains with irregular to curvilinear grain boundaries and variable grain sizes occurring in veins and altered patches of the silicate matrix

ultramafic cumulates in the Midternaes area (Szilas et al. 2014) (Fig. 1). Accepting a Mesoproterozoic or older formation age for the regional lithospheric mantle, the ca. 2 Ga model age mode obtained from olivine separates and bulk rocks in this and other studies probably reflects introduction of convecting mantle-derived, refertilising melts carrying Os and S. These model ages overlap Palaeoproterozoic Laurentian supercontinent assembly, as exemplified by the Nagssugtoqidian and Ketilidian orogens that border the GNAC to the north and south (Hoffman 1989; Garde et al. 2002). While the refertilisation and introduction of sulphides with convecting mantle-like Os is here ascribed to interaction with asthenospheric melts, S and Os introduced during the Ketilidian orogeny may have led to the addition of sulphides with radiogenic initial  $^{187}\text{Os}/^{188}\text{Os}$  (e.g. McInnes et al. 1999), which can explain the unsupported radiogenic Os of some olivine separates investigated here.

### Origin of BMS: precipitation from melt vs. capture of pre-existing alloys

The HSE systematics of olivine separates may be controlled by BMS that have captured pre-existing PGE alloys, which saturated during melt extraction in the course of lithosphere stabilisation (Griffin et al. 2002; Lorand et al. 2013). If this model is applied to the GNAC, one would expect

a greater number of BMS grains retaining Archaean ages, especially since such alloys are expected to preserve ancient  $^{187}\text{Os}/^{188}\text{Os}$  even in refertilised peridotite (Lorand et al. 2013), yet this is only true for one out of 17 BMS grains investigated by van Acken et al. (2017). Conversely, a significantly greater number of bulk rock analyses from Greenland peridotites yielded Archaean model ages and, since the majority of these samples are described as sulphide-poor or -free, this signature may be largely carried by alloys (Wittig et al. 2010).

It is interesting to note that BMS with low Os contents and radiogenic Os compositionally lie between presumably pristine BMS inclusions in peridotitic and eclogitic (i.e., metabasaltic) diamonds (Fig. 8d). Sulphides could have been introduced via a physically entrained immiscible sulphide melt with high PPGE/IPGE (Bockrath et al. 2004), or by crystallisation from sulphide melt after its exsolution from a silicate melt (Lorand et al. 2013). Although in detail, the pathway from metasomatic melt to the observed low-pressure assemblages in terms of pressure-temperature-oxygen and sulphur fugacity at each step is not known, we can attempt to reproduce the general HSE characteristics of the BMS-bearing olivine separates in our study using simple modelling. Starting from a median Pd/Ir of 4.0 for continental alkali basalts (Chu et al. 2017), a sulphide liquid exsolving from silicate melt and mss precipitating from this sulphide melt (distribution coefficients of Brenan 2008 and Mungall and Brenan 2014) would have Pd/Ir of 1.1 and 0.001, respectively (Table 5). This compares reasonably well with the average Pd/Ir of 2.3 and 0.03 for the IPGE-depleted and IPGE-rich BMS types, respectively, reported in van Acken et al. (2017). Mixtures with variable proportions of entrapped sulphide melt and mss crystallised from sulphide melt could thus explain Pd/Ir values of 0.03 to 1.25 obtained for olivine separates in this study. As the calculated sulphide liquid in equilibrium with the silicate melt has two orders of magnitude higher Ir and Pd abundances than the IPGE-depleted type reported in van Acken et al. (2017), prior precipitation of mss from the sulphide liquid is indicated, which will diminish IPGE concentrations and further increase Pd/Ir.

### Inferred and observed HSE hosts in olivine and bulk peridotite

Olivine and pyroxene separated from mantle xenoliths have highly variable HSE contents (Pearson et al. 1995; Burton et al. 2000, 2002; Lugué et al. 2009; Wittig et al. 2010; Aulbach et al. 2014; Smit et al. 2014; Pernet-Fisher et al. 2015). The low but variable contents of compatible IPGE in olivine separates may be related to the presence of discrete inclusions. This is further illustrated by a comparison to measured whole-rock peridotites from Pyramidefjeld, which

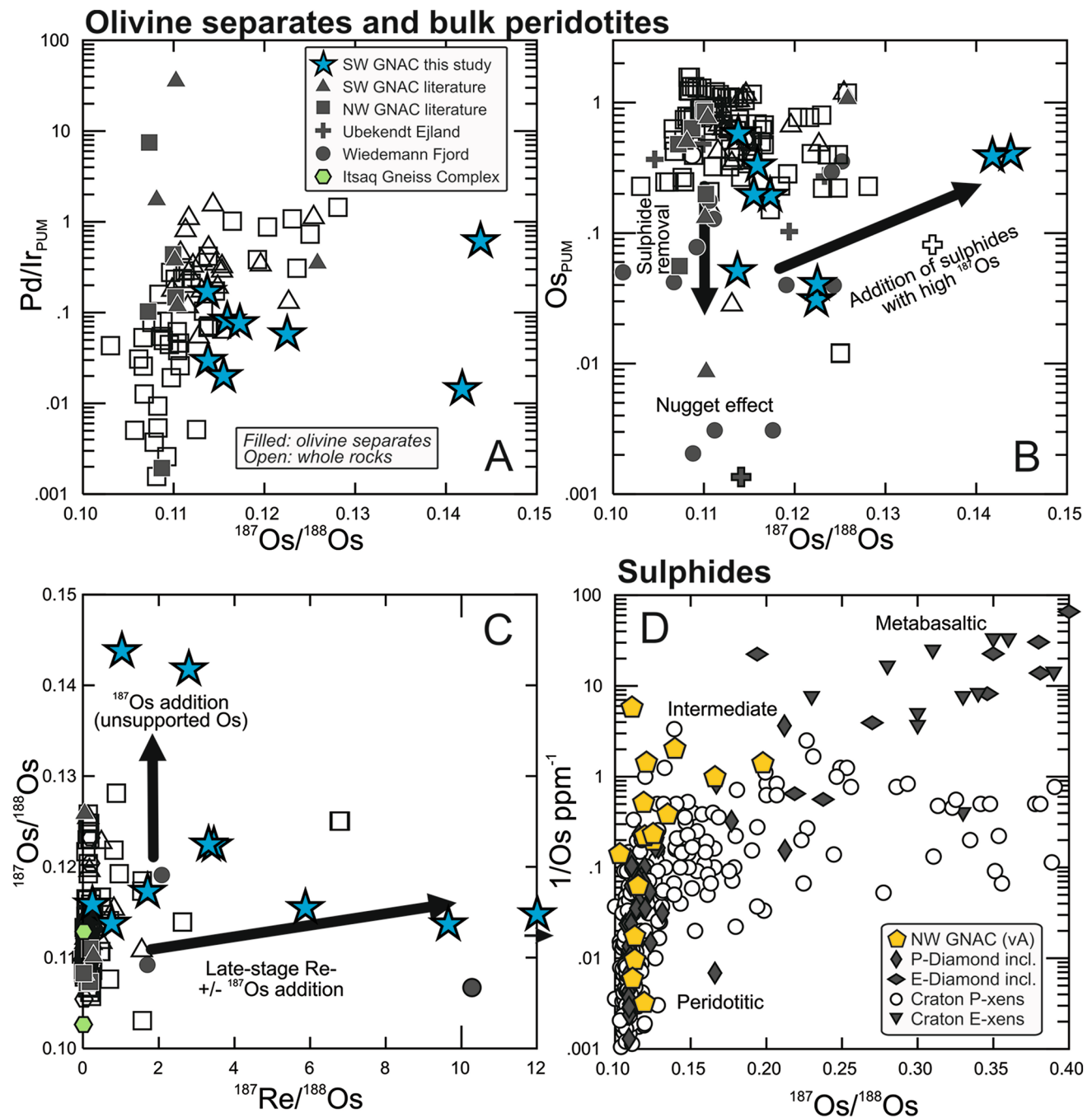


**Fig. 8** **a** Primitive Upper Mantle (PUM)-normalised Pd/Ir (PUM from Becker et al. 2006) and **b** Os as a function of  $^{187}\text{Os}/^{188}\text{Os}$ ; **c** Re–Os isochron diagram of olivine separates and whole-rocks from localities on and off cratonic Greenland (Hanghøj et al. 2001; Bennett et al. 2002; Bernstein et al. 2006; Wittig et al. 2010); **d** Re–Os isochron diagram for BMS in a mantle xenolith from Kangerlussuaq just off the NW-GNAC (“vA”; van Acken et al. 2017) as well as sulphides

included in peridotitic (P) and eclogitic/metabasaltic (E) diamond and in cratonic xenoliths (“xens”; database in Aulbach et al. 2016). In **b** sub-PUM Os concentrations in whole rocks are ascribed to loss of sulphide due to prior interaction with metasomatic melt, which conditions the lithosphere for addition of  $^{187}\text{Os}$ -rich sulphide. In **c** a qualitative arrow for late addition of Re and/or  $^{187}\text{Os}$  applies to samples with elevated  $^{187}\text{Re}/^{188}\text{Os}$  yet low  $^{187}\text{Os}/^{188}\text{Os}$

only partially overlap the HSE concentrations of HSE-rich olivine separates (Fig. 6a). The patterns are similar from Os to Pt, suggesting that this is mostly a dilution effect. This “nugget effect” hampers a direct comparison between

the composition of the olivine host and HSE systematics inferred to be largely carried by inclusions. For the Superior craton, HSE patterns for olivine from peridotite xenoliths show low Pd/Ir reminiscent of highly depleted cratonic

**Table 5** Modelling of HSE concentrations in sulphides

Sample	Material	References	Os (ppb)	Ir (ppb)	Ru (ppb)	Pt (ppb)	Pd (ppb)	Pd/Ir
<i>HSE concentrations in a mixture of average IPGE-rich and -poor sulphide compared to average olivine separates in peridotite xenoliths (this study)</i>								
474527	BMS type 1	van Acken et al. (2017)	54,014	47,957	122,714	7057	1669	0.035
474527	BMS type 2	van Acken et al. (2017)	957	919	4544	2772	2088	2.3
Calculated BMS mix	0.00002 type 1 + 0.00001 type 2		1.18	1.05	2.91	0.42	0.24	0.23
Avg this work	Olivine separate		1.20	0.78	1.35	0.49	0.18	0.23
<i>HSE concentrations in calculated sulphide liquid and mss ultimately derived from a within-plate basalt representative of a metasomatic melt</i>								
Average alkali basalt		Chu et al. (2017)		0.116	0.171	0.46	0.462	4.0
Sulphide melt/silicate liquid $D$		Mungall and Brenan (2014)		1.9E+06	4.3E+05	1.1E+06	5.4E+05	
Calculated sulphide melt				2.2E+05	7.4E+04	5.0E+05	2.5E+05	1.1
Mss/sulphide melt $D$	Experiment HP46	Brenan (2008)		7	10	0.035	0.008	
Calculated mss				1.5E+06	7.4E+05	1.8E+04	2.0E+03	0.001

mantle, and these systematics were ascribed to the presence of alloys as micro- or nano-inclusions (Smit et al. 2014). Chromite may also be a significant HSE host in peridotites. Under reducing conditions, such as apply to the cratonic mantle lithosphere, chromite strongly fractionates Ru relative to other HSE (Righter et al. 2004; Brenan et al. 2012; Park et al. 2013), but elevated normalised Ru/Ir is not clearly discernible in olivine separates investigated here, except in hercynite 4764015h1 with Ru/Ir<sub>PUM</sub> of 1.4 (Fig. 6).

Sulphides have long been known to concentrate HSE in the absence of a metal phase (Mitchell and Keays 1981; Lorand 1989; Fleet et al. 1996), and they are observed in peridotites in this study as (pseudo-)inclusions in olivine (Fig. 7e, g, h, i, j, m). PUM-normalised IPGE-patterns of olivine separates are similar to the IPGE-rich BMS type reported for a Greenland mantle peridotite xenolith (van Acken et al. 2017). Since the IPGE-rich BMS type displays much higher IPGE/PPGE than olivine separates in this study, this can be reconciled by admixing of the IPGE-depleted type. Low IPGE- (and Pt-) abundances were also determined in sulphide minerals in the present study (Fig. 4b). Minute amounts of both IPGE-rich and IPGE-poor BMS, with a total of approximately 0.01 wt% and a proportion of 1:5 broadly reproduces the average HSE abundances observed in olivine separates (Table 5). The proportion of BMS is maximum since IPGE hosted in the olivine crystal structure is not considered in the estimate (cf., Mungall and Brenan 2014). Measured BMS in this study are further characterised by high Re/Os<sub>PUM</sub> (median 16) (Fig. 4c), which can explain elevated Re/Os in olivine (3.9) and indicates that this is not due to kimberlite contamination, which affects measured bulk peridotites (e.g., Aulbach et al. 2016). Palladium, which is also enriched relative to Pt in the few sulphide minerals that could be measured, may have been added along with Re, although this did not erase the depleted HSE pattern of the

olivine separates (Fig. 6). Finally, the low Se/Te of BMS in this study compared to the majority of orogenic peridotites (Fig. 4a) is consistent with a metasomatic component, since Te behaves more incompatibly than Se (Helmy et al. 2010; König et al. 2014), leading to low Se/Te in metasomatic melts.

Interestingly, bulk peridotites from Greenland show a broad positive co-variation of  $^{187}\text{Os}/^{188}\text{Os}$  with Pd/Ir but not with  $^{187}\text{Re}/^{188}\text{Os}$ , implying coupled recent addition of Pd and radiogenic Os for the majority of samples (Fig. 8a). Olivine separates do not show this relationship. In this context, it is significant that the two BMS types described by van Acken et al. (2017)—IPGE-rich and IPGE-depleted—have similar PPGE contents, and that the latter are characterised by a depletion in the compatible IPGE rather than an enrichment in the incompatible PPGE (Fig. 6). Indistinguishable PPGE concentrations are also observed for interstitial vs. included BMS reported in Alard et al. (2000). Moreover, the more strongly metasomatised peridotite xenoliths from SW Greenland have on average higher Pd/Ir and  $^{187}\text{Os}/^{188}\text{Os}$  than those from the more depleted counterparts at the northern craton margin in West Greenland (Wittig et al. 2010) (Fig. 8a). Since Pd is incompatible in silicates and is also not alloy-forming (Mungall and Brenan 2014), these observations suggest that some Pd and  $^{187}\text{Os}$  in the bulk peridotites is hosted by a grain boundary and/or interstitial component that is not present in olivine and only accessed in bulk rock analyses. This component may be related to BMS grains or semimetal compounds such as tellurides (Helmy and Braggini 2017) that are too small for in situ analysis by laser ablation-ICPMS. This size limitation precludes a full mass balance for HSE concentration and Os isotopes in peridotite xenoliths. In addition,  $^{187}\text{Os}/^{188}\text{Os}$  is typically not reported in low-Os BMS even if they are large enough since in situ

analysis does not provide precise results, as is true also for BMS in this study.

### Effects of recurrent volatile-rich melt metasomatism on HSE- $^{187}\text{Os}$ systematics in olivine from cratonic peridotites

Continental rifting is known to facilitate the infiltration of oxidising small-volume melts (Foley 2011; Tappe et al. 2017), and in the NAC this occurred repeatedly since Palaeoproterozoic refertilisation (at 1.4–1.2 Ga, 0.61–0.55 Ga, 0.16–0.10 Ga; Tappe et al. 2007, 2012). These melts could have reached sulphide-saturation due to melt-rock reactions and decreasing melt volumes (Lorand et al. 2013), as evidenced by the high abundance of interstitial BMS in some samples (e.g., wehrlite 476407i; phl-lherzolite 476424q). In addition to the Palaeoproterozoic refertilisation discussed above, olivine Re–Os isotope systematics clearly indicate more recent disturbance of the system (Fig. 8c). This may have occurred during rifting, decompression and associated metasomatism of the cratonic mantle lithosphere, as reflected in phlogopite and cpx addition from small-volume oxidising melts shortly before kimberlite eruption at ca. 150 Ma, accompanied by lower contents of V which behaved more incompatibly during oxidising metasomatism (Aulbach et al. 2017).

Wehrlite 476407i is exceptionally BMS-rich, containing large grains and a multitude of medium and small grains, both as pseudo-inclusions within olivine crystals and at grain boundaries (Fig. 7a–d). Olivine in this sample not only has the highest Re content, but also some of the lowest HSE contents and the lowest  $^{187}\text{Os}/^{188}\text{Os}$  in the suite. Rhenium liberated during extension-related garnet breakdown, as observed in the peridotite xenolith suite under investigation (Aulbach et al. 2017), especially under oxidising conditions (Righter et al. 2008), may be responsible for the addition of Re-rich (but Os-poor) components to portions of the mantle section, explaining the association of high Re/Os with unradiogenic Os in some olivine separates. Conversely, radiogenic Os ( $^{187}\text{Os}/^{188}\text{Os} > 0.14$ ), unsupported by the amount of Re measured, is observed in three olivine separates, from both cryptically and modally metasomatised samples (two lherzolites and a phl-wehrlite), which also have some of the highest Os concentrations in the sample suite. This requires interaction with a metasomatic agent that inherited radiogenic Os from an enriched and aged lithospheric source. Sulphides precipitating early from sulphide melts exsolved from such metasomatic agents would scavenge the compatible Os and control the Os isotopic composition in those parts of the mantle lithosphere that had lost earlier sulphide generations (and potentially alloys). This suggested two-step process is illustrated in Fig. 8b. Although alloys are generally long-lived and robust (e.g., Pearson et al. 2007), their behaviour

in equilibrium with melt is dictated by their solubility, which increases in the presence of S in the melt (e.g., from earlier dissolution of BMS) and with increasing  $f_{\text{O}_2}$  (Mungall and Brenan 2014), which may facilitate their (partial) removal. Alternatively, rather than by direct dissolution, they may be removed as sulphides after having been re-dissolved in metasomatic BMS (Griffin et al. 2002).

While depletions of the IPGE in olivine separates may reflect nugget effects, combined with the fact that olivine alone does not account for whole-rock HSE contents, as discussed above, the majority of bulk peridotites from Greenland also show significant HSE depletions relative to PUM (Fig. 9a, b). We suggest that this reflects BMS removal during recurrent oxidative melt metasomatism, as must have occurred beneath cratonic Greenland judging from the high frequency of Neoproterozoic and Mesozoic alkaline and carbonatite magmatic activity (Tappe et al. 2012, 2017). This loss may have been mediated by physical remobilisation or dissolution of BMS in S-undersaturated melts (Lorand et al. 2003; Gonzalez-Jimenez et al. 2014), aided by the presence of water (from which metasomatic phlogopite precipitated) and oxidising conditions, both of which are linked to an increase the S solubility in silicate melts (Jugo 2009; Fortin et al. 2015). It is here assumed that this is also true for carbonated silicate melts, such as kimberlites, where corresponding HSE enrichments have been ascribed to oxidative assimilation at mantle depth (Aulbach et al. 2016). Percolation of small-volume volatile-rich melts similar to carbonatite in peridotite xenoliths from Montferrier in southern France resulted in addition of metasomatic BMS and supra-PUM HSE concentrations in the bulk rock (Alard et al. 2011). This may speak to even more efficient scavenging of HSE-rich minerals by carbonatite followed by deposition during metasomatism, compared to the carbonated silicate melts implied in the mantle metasomatism beneath the SW-GNAC.

The process of BMS removal is envisaged as progressive, meaning that some BMS may be inherited from older events, whereas others reflect re-introduction of HSE-poor sulphides, as discussed above. None of the olivine separates in this study yielded Archaean ages and only four of 23 peridotite samples (including three of four olivine separates) in the study of Wittig et al. (2010) give Archaean  $T_{\text{RD}}$ , between 2.5 and 2.8 Ga. This scarcity of Archaean Re–Os model ages in SW-GNAC mantle samples may result from the efficient removal of older sulphides (and potentially alloys). The absence of any vestige of the original Mesoarchaean or older melt depletion event in the Re–Os isotope compositions of olivine separates from very fresh peridotite xenoliths in this study suggests that similar results obtained by Wittig et al. (2010) for the majority of highly serpentinised bulk peridotite samples from the same locality are not due to extensive alteration in the surface environment, but rather to stripping

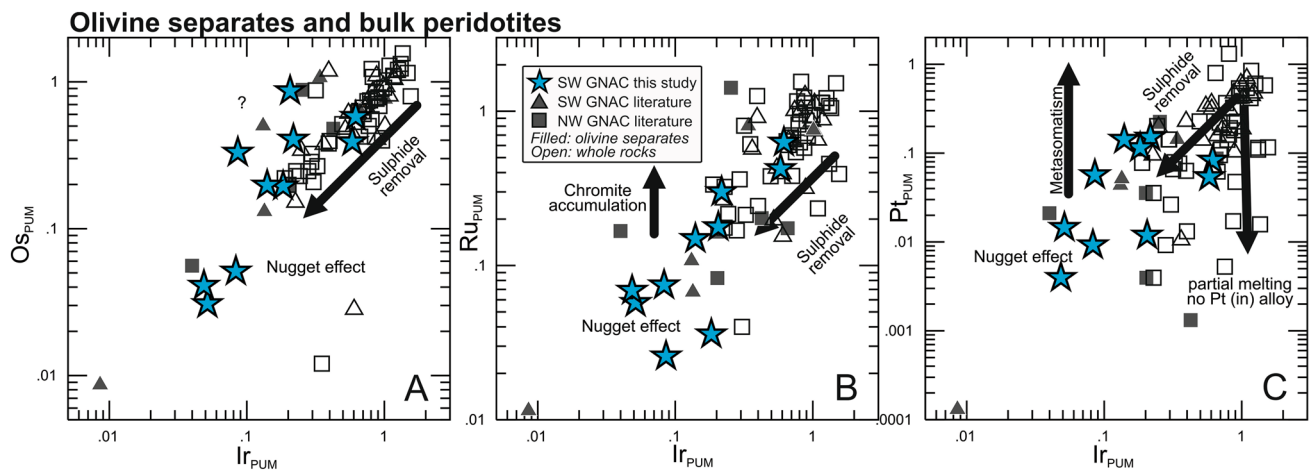


**Fig. 9** Primitive Upper Mantle (PUM)-normalised HSE abundances for olivine separates and whole rocks from localities on and off cratonic Greenland (references as in Fig. 8). In **a** several olivine fractions and a whole rock from the GNAC have conspicuously high Os/Ir, the origin of which is, however, unclear. Arrows in **a–c** show qualitative trends for sub-PUM HSE abundances due to nugget effect (amount and type of sulphides or alloys in olivine) or due to loss of sulphide

or alloy, which would have saturated after melt extraction leading to lithosphere stabilisation in the Archaean (whole rocks and olivine separates); arrow in **b** indicates the effect of chromite accumulation (e.g., during metasomatism) leading to elevated Ru/Ir; arrow in **c** indicates the effect of Pt alloy saturation or lack thereof during melt extraction, which determines the amount of Pt remaining in the residue (Mungall and Brenan 2014). See text for details

and overprinting of the HSE systematics in the presence of migrating carbonate-rich melts at mantle depth. Thus, distinguishing Proterozoic Os model ages for mantle xenoliths in terms of original lithosphere stabilisation in the Proterozoic (e.g., Liu et al. 2018) vs. nearly complete isotopic re-setting of originally older lithosphere, as inferred here, remains a challenge.

## Summary and conclusions

We determined HSE concentrations and Re–Os isotope compositions of olivine separates from variably metasomatised peridotite xenoliths (reaction dunite, lherzolites, phl-wehrlites) from the ca. 150 Ma Pyramidefjeld and Midternaes kimberlites on the southern margin of the North Atlantic craton in SW Greenland. We also investigated in detail the mineralogy and major- and trace element compositions of BMS occurring in these mantle-derived rocks. Combined with literature data for peridotite xenoliths from this and other localities on and off the GNAC, the following conclusions can be drawn regarding the chemical, physical and mineralogical effects of recurrent rifting and associated volatile-rich melt percolation in the regional lithospheric mantle:

- Refertilised lherzolites are dominated by rare to frequent small ( $\leq$  tens of  $\mu\text{m}$ ) BMS inclusions in olivine, whereas modally metasomatised phl-lherzolite and two of three wehrlites additionally contain abundant large

(hundreds of  $\mu\text{m}$ ) interstitial grains. Olivine separates display depleted HSE systematics regardless of host rock lithology, with Pd/Ir<sub>PUM</sub> of 0.014–0.62, but have both depleted and enriched  $^{187}\text{Os}/^{188}\text{Os}$  (0.1139–0.2724) that are not correlated with  $^{187}\text{Re}/^{188}\text{Os}$ . Compatible IPGE are conspicuously depleted in all but one olivine separate ( $< 0.5 \times \text{PUM}$  for Ru, Ir, Os).

- Four out of ten olivine separates have similar unradiogenic  $^{187}\text{Os}/^{188}\text{Os}$  (0.1139–0.1163) with Re-depletion model ages of 2.1–1.8 Ga. This may reflect refertilisation (lherzolitisation) during the Palaeoproterozoic Laurentia plate assembly, with re-introduction of clinopyroxene and IPGE-rich BMS into the originally refractory, clinopyroxene- and sulphide-free mantle lithosphere, by precipitation from sulphide melts separating from asthenosphere-derived silicate melts. This was followed by recrystallisation and occlusion in olivine.
- Unradiogenic Os is observed regardless of host rock lithology, including in olivine separates from samples with abundant interstitial BMS. This signature is suggested to be controlled by Os-rich BMS that precipitated from sulphide melt after its exsolution from the refertilising silicate melt, whereas BMS added during more recent wehrlitisation and phlogopite-introduction is Os-poor, probably due to direct entrapment of melt and/or prior fractional crystallisation of BMS scavenging Os.
- While depletions in the compatible IPGE in all but one olivine separate may reflect nugget effects (amount and type of BMS inclusion, depleted vs. metasomatic), similar depletions observed in bulk peridotite xenoliths from

the same area are ascribed to sulphide removal due to partial dissolution into oxidising small-volume melts that migrated through the lithosphere during recurrent rifting, and finally replacement by HSE-poor BMS when metasomatic melts reached sulphide-saturation.

- Recent extension-related garnet breakdown leading to Re liberation, and precipitation of BMS from metasomatic melts originating in aged lithospheric metasomes, may explain disturbed Re–Os isotope systematics (high Re/Os at depleted  $^{187}\text{Os}/^{188}\text{Os}$  and unsupported radiogenic  $^{187}\text{Os}/^{188}\text{Os}$  at high Os concentrations, respectively).

Combined, multiple oxidative metasomatic events and the effects of the Ketilidian orogeny at the southwestern craton margin destroyed most vestiges of a Mesoarchean or older inheritance in the samples investigated here as well as those reported for this region in the literature, potentially including removal of long-lived alloys that would have saturated during strong melt depletion associated with Archaean lithosphere formation.

**Acknowledgements** We thank Maximilian Engel and Theodoros Potouridis for help with sulphide characterisation and the high-pressure asher, respectively. Troels Nielsen is gratefully acknowledged for making the specimens available from the GEUS rock storage facility. Incisive and constructive reviews by Kristoffer Szilas and an anonymous reviewer as well as editorial comments by Chris Ballhaus greatly improved the manuscript. The German Research Foundation (DFG) is thanked for support under grant GE1152/9. Part of this work was carried out during JS's research stay in Germany, which was supported by the German Academic Exchange Service (DAAD). ST acknowledges support by the Geological Survey of Denmark and Greenland, and by the DST-NRF CIMERA Centre of Excellence at the University of Johannesburg, South Africa.

## References

- Alard O, Griffin WL, Lorand JP, Jackson SE, O'Reilly SY (2000) Non-chondritic distribution of the highly siderophile elements in mantle sulphides. *Nature* 407(6806):891–894
- Alard O, Lorand JP, Reisberg L, Bodinier JL, Dautria JM, O'Reilly SY (2011) Volatile-rich metasomatism in montferrier xenoliths (Southern France): implications for the abundances of chalcophile and highly siderophile elements in the subcontinental mantle. *J Petrol* 52(10):2009–2045. <https://doi.org/10.1093/ptrology/egr038>
- Arndt NT, Guitreau M, Boullier AM, Le Roex A, Tommasi A, Cordier P, Sobolev A (2010) Olivine, and the origin of kimberlite. *J Petrol* 51(3):573–602. <https://doi.org/10.1093/ptrology/egp080>
- Aulbach S (2019) Cratonic Lithosphere Discontinuities: Dynamics of Small-Volume Melting, Meta-Cratonisation and a Possible Role for Brines. In: Yuan H, Romanowicz B (eds) *Lithospheric discontinuities*. Geophysical monograph, vol 239. American Geophysical Union, Washington DC, pp 177–204
- Aulbach S, Stachel T, Creaser RA, Heaman LM, Shirey SB, Muehlenbachs K, Eichenberg D, Harris JW (2009) Sulphide survival and diamond genesis during formation and evolution of Archaean subcontinental lithosphere: a comparison between the Slave and Kaapvaal cratons. *Lithos* 112:747–757. <https://doi.org/10.1016/j.lithos.2009.03.048>
- Aulbach S, Stachel T, Seitz H-M, Brey GP (2012) Chalcophile and siderophile elements in sulphide inclusions in eclogitic diamonds and metal cycling in a Paleoproterozoic subduction zone. *Geochim Cosmochim Acta* 93:278–299. <https://doi.org/10.1016/j.gca.2012.04.027>
- Aulbach S, Luchs T, Brey GP (2014) Distribution and behaviour during metamorphism of PGE-Re and Os isotopes in off-craton mantle xenoliths from Namibia. *Lithos* 184:478–490. <https://doi.org/10.1016/j.lithos.2013.09.003>
- Aulbach S, Mungall JE, Pearson DG (2016) Distribution and processing of highly siderophile elements in cratonic mantle lithosphere. In: Harvey J, Day JMD (eds) *Highly siderophile and strongly chalcophile elements in high-temperature geochemistry and cosmochemistry*, vol 81. Mineralogical Society of America, USA, pp 239–304
- Aulbach S, Sun J, Tappe S, Hofer HE, Gerdes A (2017) Volatile-rich metasomatism in the cratonic mantle beneath SW Greenland: link to kimberlites and mid-lithospheric discontinuities. *J Petrol* 58(12):2311–2338. <https://doi.org/10.1093/ptrology/egy009>
- Becker H, Horan MF, Walker RJ, Gao S, Lorand J-P, Rudnick RL (2006) Highly siderophile element composition of the Earth's primitive upper mantle: constraints from new data on peridotite massifs and xenoliths. *Geochim Cosmochim Acta* 70(17):4528–4550
- Bennett VC, Nutman AP, Esat TM (2002) Constraints on mantle evolution from Os-187/Os-188 isotopic compositions of Archean ultramafic rocks from southern West Greenland (3.8 Ga) and Western Australia (3.46 Ga). *Geochim Cosmochim Acta* 66(14):2615–2630. [https://doi.org/10.1016/s0016-7037\(02\)00862-1](https://doi.org/10.1016/s0016-7037(02)00862-1)
- Bennett VC, Brandon AD, Nutman AP (2007) Coupled Nd-142-Nd-143 isotopic evidence for Hadean mantle dynamics. *Science* 318(5858):1907–1910. <https://doi.org/10.1126/science.1145928>
- Bernstein S, Kelemen PB, Brooks CK (1998) Depleted spinel harzburgite xenoliths in tertiary dykes from east Greenland: restites from high degree melting. *Earth Planet Sci Lett* 154(1–4):221–235
- Bernstein S, Hanghoj K, Kelemen PB, Brooks CK (2006) Ultra-depleted, shallow cratonic mantle beneath West Greenland: dunitic xenoliths from Ubekendt Eiland. *Contrib Mineral Petrol* 152(3):335–347. <https://doi.org/10.1007/s00410-006-0109-0>
- Bernstein S, Kelemen PB, Hanghoj K (2007) Consistent olivine Mg# in cratonic mantle reflects Archean mantle melting to the exhaustion of orthopyroxene. *Geology* 35(5):459–462. <https://doi.org/10.1130/g23336a.1>
- Bernstein S, Szilas K, Kelemen PB (2013) Highly depleted cratonic mantle in West Greenland extending into diamond stability field in the Proterozoic. *Lithos* 168:160–172. <https://doi.org/10.1016/j.lithos.2013.02.011>
- Bizzarro M, Stevenson RK (2003) Major element composition of the lithospheric mantle under the North Atlantic craton: evidence from peridotite xenoliths of the Sarfartoq area, southwestern Greenland. *Contrib Mineral Petrol* 146(2):223–240. <https://doi.org/10.1007/s00410-003-0499-1>
- Bockrath C, Ballhaus C, Holzheid A (2004) Fractionation of the platinum-group elements during mantle melting. *Science* 305(5692):1951–1953
- Brenan JM (2008) Re–Os fractionation by sulfide melt-silicate melt partitioning: a new spin. *Chem Geol* 248(3–4):140–165. <https://doi.org/10.1016/j.chemgeo.2007.09.003>
- Brenan JM, Finnigan CF, McDonough WF, Homolova V (2012) Experimental constraints on the partitioning of Ru, Rh, Ir, Pt and Pd between chromite and silicate melt: the importance of ferric iron. *Chem Geol* 302:16–32

- Burton KW, Schiano P, Birck JL, Allegre CJ, Rehkamper M, Halliday AN, Dawson JB (2000) The distribution and behaviour of rhenium and osmium amongst mantle minerals and the age of the lithospheric mantle beneath Tanzania. *Earth Planet Sci Lett* 183(1–2):93–106
- Burton KW, Gannoun A, Birck JL, Allegre CJ, Schiano P, Clocchiatti R, Alard O (2002) The compatibility of rhenium and osmium in natural olivine and their behaviour during mantle melting and basalt genesis. *Earth Planet Sci Lett* 198(1–2):63–76. [https://doi.org/10.1016/s0012-821x\(02\)00518-6](https://doi.org/10.1016/s0012-821x(02)00518-6)
- Chu ZY, Yan Y, Zeng G, Tian W, Li CF, Yang YH, Guo JH (2017) Petrogenesis of Cenozoic basalts in central-eastern China: constraints from Re–Os and PGE geochemistry. *Lithos* 278:72–83. <https://doi.org/10.1016/j.lithos.2017.01.022>
- Coggon JA, Luguet A, Nowell GM, Appel PWU (2013) Hadean mantle melting recorded by southwest Greenland chromitite Os-186 signatures. *Nat Geosci* 6(10):871–874. <https://doi.org/10.1038/ngeo1911>
- Craig JR (1973) Pyrite-pentlandite assemblages and other low-temperature relations in Fe–Ni–S system. *Am J Sci* A273:496–510
- Emeleus CH, Andrews JR (1975) Mineralogy and petrology of kimberlite dyke and sheet intrusions and included peridotite xenoliths from south-west Greenland. *Phys Chem Earth* 9:179–198
- Fleet ME, Crocket JH, Stone WE (1996) Partitioning of platinum-group elements (Os, Ir, Ru, Pt, Pd) and gold between sulfide liquid and basalt melt. *Geochim Cosmochim Acta* 60(13):2397–2412. [https://doi.org/10.1016/0016-7037\(96\)00100-7](https://doi.org/10.1016/0016-7037(96)00100-7)
- Foley SF (2011) A reappraisal of redox melting in the Earth's mantle as a function of tectonic setting and time. *J Petrol* 52(7–8):1363–1391. <https://doi.org/10.1093/petrology/egg061>
- Fortin MA, Riddle J, Desjardins-Langlais Y, Baker DR (2015) The effect of water on the sulfur concentration at sulfide saturation (SCSS) in natural melts. *Geochim Cosmochim Acta* 160:100–116. <https://doi.org/10.1016/j.gca.2015.03.022>
- Frei D, Hutchison MT, Gerdes A, Heaman LM (2008) Common-lead corrected U–Pb age dating of perovskite by laser ablation—magnetic sectorfield ICP-MS. In: 9th international kimberlite conference, vol extended abstract. Frankfurt am Main, Germany, p 9IKC-A-00216
- Garde AA, Hamilton MA, Chadwick B, Grocott J, McCaffrey KJW (2002) The Ketilidian orogen of South Greenland: geochronology, tectonics magmatism and fore-arc accretion during Palaeoproterozoic oblique convergence. *Can J Earth Sci* 39(5):765–793
- Godel B, Barnes SJ (2008) Platinum-group elements in sulfide minerals and the whole rocks of the J-M Reef (Stillwater Complex): implication for the formation of the reef. *Chem Geol* 248(3–4):272–294. <https://doi.org/10.1016/j.chemgeo.2007.05.006>
- Gonzalez-Jimenez JM, Villaseca C, Griffin WL, O'Reilly SY, Belousova E, Ancochea E, Pearson NJ (2014) Significance of ancient sulfide PGE and Re–Os signatures in the mantle beneath Calatrava, Central Spain. *Contrib Mineral Petrol*. <https://doi.org/10.1007/s00410-014-1047-x>
- Griffin WL, Spetsius ZV, Pearson NJ, O'Reilly SY (2002) In situ Re–Os analysis of sulfide inclusions in kimberlitic olivine: new constraints on depletion events in the Siberian lithospheric mantle. *Geochem Geophys Geosyst* 3:1069
- Griffin WL, O'Reilly SY, Doyle BJ, Pearson NJ, Coopersmith H, Kivi K, Malkovets V, Pokhilenko N (2004) Lithosphere mapping beneath the north American plate. *Lithos* 77(1–4):873–922. <https://doi.org/10.1016/j.lithos.2004.03.034>
- Griffin WL, Powell WJ, Pearson NJ, O'Reilly SY (2008) A2. GLITTER: data reduction software for laser ablation ICP-MS. In: Sylvester P (ed) *Laser ablation-ICPMS in the Earth sciences: current practices and outstanding issues*, vol 40. Mineralogical Association of Canada, Vancouver, p 356
- Hanhøj K, Kelemen P, Bernstein S, Blusztajn J, Frei R (2001) Osmium isotopes in the Wiedemann Fjord mantle xenoliths: a unique record of cratonic mantle formation by melt depletion in the Archaean. *Geochem Geophys Geosyst* 2:2000GC000085
- Helmy HM, Bragagni A (2017) Platinum-group elements fractionation by selective complexing, the Os, Ir, Ru, Rh-arsenide-sulfide systems above 1020 degrees C. *Geochim Cosmochim Acta* 216:169–183. <https://doi.org/10.1016/j.gca.2017.01.040>
- Helmy HM, Ballhaus C, Wohlgenuth-Ueberwasser C, Fonseca ROC, Laurenz V (2010) Partitioning of Se, As, Sb, Te and Bi between monosulfide solid solution and sulfide melt—application to magmatic sulfide deposits. *Geochim Cosmochim Acta* 74(21):6174–6179. <https://doi.org/10.1016/j.gca.2010.08.009>
- Hoffman PF (1989) Precambrian geology and tectonic history of North America. In: Bally AW, Palmer AR (eds) *The geology of North America—an overview*, vol Geological Society of America, Boulder, pp 447–512
- Horan MF, Walker RJ, Morgan JW, Grossman JN, Rubin AE (2003) Highly siderophile elements in chondrites. *Chem Geol* 196(1–4):5–20. [https://doi.org/10.1016/s0009-2541\(02\)00405-9](https://doi.org/10.1016/s0009-2541(02)00405-9)
- Hutchison MT, Heaman LM (2008) Chemical and physical characteristics of diamond crystals from Garnet Lake, Sarfartoq, West Greenland: an association with carbonatitic magmatism. *Can Mineral* 46:1063–1078. <https://doi.org/10.3749/canmin.46.4.1063>
- Hutchison MT, Nielsen LJ, Bernstein S (2007) P-T history of kimberlite-hosted garnet lherzolites from South-West Greenland. *Geol Surv Den Greenl Bull* 13:45–48
- Jugo PJ (2009) Sulfur content at sulfide saturation in oxidized magmas. *Geology* 37(5):415–418. <https://doi.org/10.1130/g25527a.1>
- Keays RR (1995) The role of komatiitic and picritic magmatism and S-saturation in the formation of ore-deposits. *Lithos* 34(1–3):1–18
- König S, Lorand JP, Luguet A, Pearson DG (2014) A non-primitive origin of near-chondritic S–Se–Te ratios in mantle peridotites; implications for the Earth's late accretionary history. *Earth Planet Sci Lett* 385:110–121. <https://doi.org/10.1016/j.epsl.2013.10.036>
- Larsen LM, Heaman LM, Creaser RA, Duncan RA, Frei R, Hutchison M (2009) Tectonomagmatic events during stretching and basin formation in the Labrador Sea and the Davis Strait: evidence from age and composition of Mesozoic to Palaeogene dyke swarms in West Greenland. *J Geol Soc* 166:999–1012. <https://doi.org/10.1144/0016-76492009-038>
- Liu J, Brin LE, Pearson DG, Bretschneider L, Luguet A, van Acken D, Kjarsgaard B, Riches A, Mišković A (2018) Diamondiferous Paleoproterozoic mantle roots beneath Arctic Canada: a study of mantle xenoliths from Parry Peninsula and Central Victoria Island. *Geochim Cosmochim Acta* 239:284–311
- Lorand JP (1989) Sulfide petrology of spinel and garnet pyroxenite layers from mantle-derived spinel lherzolite massifs of Ariège, Northeastern Pyrenees, France. *J Petrol* 30(4):987–1015
- Lorand JP, Grégoire M (2006) Petrogenesis of base metal sulphide assemblages of some peridotites from the Kaapvaal craton (South Africa). *Contrib Mineral Petrol* 151(5):521–538. <https://doi.org/10.1007/s00410-006-0074-7>
- Lorand JP, Reisberg L, Bedini RM (2003) Platinum-group elements and melt percolation processes in Sidam spinel peridotite xenoliths, Ethiopia, East African Rift. *Chem Geol* 196(1–4):57–75. [https://doi.org/10.1016/s0009-2541\(02\)00407-2](https://doi.org/10.1016/s0009-2541(02)00407-2)
- Lorand JP, Luguet A, Alard O (2013) Platinum-group element systematics and petrogenetic processing of the continental upper mantle: a review. *Lithos* 164:2–21. <https://doi.org/10.1016/j.lithos.2012.08.017>
- Luguet A, Alard O, Lorand JP, Pearson NJ, Ryan C, O'Reilly SY (2001) Laser-ablation microprobe (LAM)-ICPMS unravels the highly siderophile element geochemistry of the oceanic mantle. *Earth Planet Sci Lett* 189(3–4):285–294

- Luguet A, Jaques AL, Pearson DG, Smith CB, Bulanova GP, Rofey SL, Rayner MJ, Lorand JP (2009) An integrated petrological, geochemical and Re–Os isotope study of peridotite xenoliths from the Argyle lamproite, Western Australia and implications for cratonic diamond occurrences. *Lithos* 112:1096–1108. <https://doi.org/10.1016/j.lithos.2009.05.022>
- McInnes BIA, McBride JS, Evans NJ, Lambert DD, Andrew AS (1999) Osmium isotope constraints on ore metal recycling in subduction zones. *Science* 286(5439):512–516
- Meisel T, Moser J (2004) Reference materials for geochemical PGE analysis: new analytical data for Ru, Rh, Pd, Os, Ir, Pt and Re by isotope dilution ICP-MS in 11 geological reference materials. *Chem Geol* 208(1–4):319–338. <https://doi.org/10.1016/j.chemgeo.2004.04.019>
- Meisel T, Walker RJ, Irving AJ, Lorand J-P (2001) Osmium isotopic compositions of mantle xenoliths: a global perspective. *Geochim Cosmochim Acta* 65(8):1311–1323
- Meisel T, Fellner N, Moser J (2003) A simple procedure for the determination of platinum group elements and rhenium (Ru, Rh, Pd, Re, Os, Ir and Pt) using ID-ICP-MS with an inexpensive on-line matrix separation in geological and environmental materials. *J Anal At Spectrom* 18(7):720–726. <https://doi.org/10.1039/b301754k>
- Mitchell RH, Keays RR (1981) Abundance and distribution of gold, palladium and iridium in some spinel and garnet lherzolites—implications for the nature and origin of precious metal-rich intergranular components in the upper mantle. *Geochim Cosmochim Acta* 45(12):2425–2442. [https://doi.org/10.1016/0016-7037\(81\)90096-x](https://doi.org/10.1016/0016-7037(81)90096-x)
- Mungall JE, Brenan JM (2014) Partitioning of platinum-group elements and Au between sulfide liquid and basalt and the origins of mantle-crust fractionation of the chalcophile elements. *Geochim Cosmochim Acta* 125:265–289. <https://doi.org/10.1016/j.gca.2013.10.002>
- Nielsen LJ, Hutchison MT, Malarkey J (2008) Geothermal constraints from kimberlite-hosted garnet lherzolites from southern Greenland. In: 9th International Kimberlite conference, Frankfurt, Germany, p 9IKC-A-00047
- Nilsson MKM, Klausen MB, Söderlund U, Ernst RE (2013) Precise U–Pb ages and geochemistry of Palaeoproterozoic mafic dykes from southern West Greenland: linking the North Atlantic and the Dharwar. *Lithos* 174:255–270
- Park J-W, Campbell IH, Arculus RJ (2013) Platinum-alloy and sulfur saturation in an arc-related basalt to rhyolite suite: evidence from the Pual Ridge lavas, the Eastern Manus Basin. *Geochim Cosmochim Acta* 101:76–95. <https://doi.org/10.1016/j.gca.2012.10.001>
- Pearson DG, Wittig N (2008) Formation of Archaean continental lithosphere and its diamonds: the root of the problem. *J Geol Soc* 165:895–914
- Pearson DG, Wittig N (2014) The formation and evolution of cratonic mantle lithosphere—evidence from mantle xenoliths. In: Holland HD, Turekian KK (eds) *Treatise on geochemistry*, vol 2. Elsevier Ltd., Amsterdam, pp 255–292
- Pearson DG, Shirey SB, Carlson RW, Boyd FR, Pokhilenko NP, Shimizu N (1995) Re–Os, Sm–Nd, and Rb–Sr isotope evidence for thick Archean lithospheric mantle beneath the Siberian craton modified by multistage metasomatism. *Geochim Cosmochim Acta* 59(5):959–977
- Pearson DG, Parman SW, Nowell GM (2007) A link between large mantle melting events and continent growth seen in osmium isotopes. *Nature* 449(7159):202–205. <https://doi.org/10.1038/nature06122>
- Pernet-Fisher JF, Howarth GH, Pearson DG, Woodland S, Barry PH, Pokhilenko NP, Pokhilenko LN, Agashev AM, Taylor LA (2015) Plume impingement on the Siberian SCLM: Evidence from Re–Os isotope systematics. *Lithos* 218:141–154. <https://doi.org/10.1016/j.lithos.2015.01.010>
- Righter K, Campbell AJ, Humayun M, Hervig RL (2004) Partitioning of Ru, Rh, Pd, Re, Ir, and Au between Cr-bearing spinel, olivine, pyroxene and silicate melts. *Geochim Cosmochim Acta* 68(4):867–880. <https://doi.org/10.1016/j.gca.2003.07.005>
- Righter K, Chesley JT, Calazza CM, Gibson EK Jr, Ruiz J (2008) Re and Os concentrations in arc basalts: the roles of volatility and source region fO(2) variations. *Geochim Cosmochim Acta* 72(3):926–947. <https://doi.org/10.1016/j.gca.2007.11.024>
- Sand KK, Waight TE, Pearson DG, Nielsen TFD, Makovicky E, Hutchison MT (2009) The lithospheric mantle below southern West Greenland: a geothermobarometric approach to diamond potential and mantle stratigraphy. *Lithos* 112:1155–1166. <https://doi.org/10.1016/j.lithos.2009.05.012>
- Shirey SB, Walker RJ (1998) The Re–Os isotope system in cosmochemistry and high-temperature geochemistry. *Annu Rev Earth Planet Sci* 26:423–500. <https://doi.org/10.1146/annurev.earth.26.1.423>
- Smit KV, Pearson DG, Stachel T, Seller M (2014) Peridotites from Attawapiskat, Canada: mesoproterozoic reworking of Palaeoarchaean lithospheric mantle beneath the northern superior superterrane. *J Petrol* 55(9):1829–1863. <https://doi.org/10.1093/ptrology/egu043>
- Szilas K, Van Hinsberg VJ, Creaser RA, Kisters AFM (2014) The geochemical composition of serpentinites in the Mesoarchaean Tartuq Group, SW Greenland: Harzburgitic cumulates or melt-modified mantle? *Lithos* 198:103–116. <https://doi.org/10.1016/j.lithos.2014.03.024>
- Tappe S, Foley SF, Stracke A, Romer RL, Kjarsgaard BA, Heaman LM, Joyce N (2007) Craton reactivation on the Labrador Sea margins: 40Ar/39Ar age and Sr–Nd–Hf–Pb isotope constraints from alkaline and carbonatite intrusives. *Earth Planet Sci Lett* 256(3–4):433–454. <https://doi.org/10.1016/j.epsl.2007.01.036>
- Tappe S, Foley SF, Kjarsgaard BA, Romer RL, Heaman LM, Stracke A, Jenner GA (2008) Between carbonatite and lamproite—diamondiferous Torngat ultramafic lamprophyres formed by carbonate-fluxed melting of cratonic MARID-type metasomes. *Geochim Cosmochim Acta* 72(13):3258–3286. <https://doi.org/10.1016/j.gca.2008.03.008>
- Tappe S, Smart KA, Pearson DG, Steenfelt A, Simonetti A (2011a) Craton formation in Late Archean subduction zones revealed by first Greenland eclogites. *Geology* 39:1103–1106
- Tappe S, Pearson DG, Nowell G, Nielsen T, Milstead P, Muehlenbachs K (2011b) A fresh isotopic look at Greenland kimberlites: cratonic mantle lithosphere imprint on deep source signal. *Earth Planet Sci Lett* 305(1–2):235–248. <https://doi.org/10.1016/j.epsl.2011.03.005>
- Tappe S, Steenfelt A, Nielsen T (2012) Asthenospheric source of Neoproterozoic and Mesozoic kimberlites from the North Atlantic craton, West Greenland: new high-precision U–Pb and Sr–Nd isotope data on perovskite. *Chem Geol* 320:113–127. <https://doi.org/10.1016/j.chemgeo.2012.05.026>
- Tappe S, Romer RL, Stracke A, Steenfelt A, Smart KA, Muehlenbachs K, Torsvik TH (2017) Sources and mobility of carbonate melts beneath cratons, with implications for deep carbon cycling, metasomatism and rift initiation. *Earth Planet Sci Lett* 466:152–167. <https://doi.org/10.1016/j.epsl.2017.03.011>
- van Acken D, Becker H, Walker RJ, McDonough WF, Wombacher F, Ash RD, Piccoli PM (2010) Formation of pyroxenite layers in the Totalp ultramafic, massif (Swiss Alps)—insights from highly siderophile elements and Os isotopes. *Geochim Cosmochim Acta* 74(2):661–683. <https://doi.org/10.1016/j.gca.2009.10.007>
- van Acken D, Luguet A, Pearson DG, Nowell GM, Fonseca ROC, Nagel TJ, Schulz T (2017) Mesoarchaean melting and Neoproterozoic

- to Paleoproterozoic metasomatism during the formation of the cratonic mantle keel beneath West Greenland. *Geochim Cosmochim Acta* 203:37–53. <https://doi.org/10.1016/j.gca.2017.01.006>
- Wainwright AN, Lugué A, Fonseca ROC, Pearson DG (2015) Investigating metasomatic effects on the Os-187 isotopic signature: a case study on micrometric base metal sulphides in metasomatised peridotite from the Letlhakane kimberlite (Botswana). *Lithos* 232:35–48. <https://doi.org/10.1016/j.lithos.2015.06.017>
- Walter MJ (2014) Melt extraction and compositional variability in mantle lithosphere. In: Holland HD, Turekian KK, Carlson RW (eds) *Treatise on geochemistry* (2nd edition) volume 3: the mantle and the core, vol 3. Elsevier Pergamon, Amsterdam, pp 393–419
- Wilson SA, Ridley WI, Koenig AE (2002) Development of sulfide calibration standards for the laser ablation inductively-coupled plasma mass spectrometry technique. *J Anal At Spectrom* 17(4):406–409. <https://doi.org/10.1039/b108787h>
- Windley BF, Garde AA (2009) Arc-generated blocks with crustal sections in the North Atlantic craton of West Greenland: crustal growth in the Archean with modern analogues. *Earth Sci Rev* 93(1–2):1–30. <https://doi.org/10.1016/j.earscirev.2008.12.001>
- Wittig N, Pearson DG, Webb M, Ottley CJ, Irvine GJ, Kopylova M, Jensen SM, Nowell GM (2008) Origin of cratonic lithospheric mantle roots: a geochemical study of peridotites from the North Atlantic Craton, West Greenland. *Earth Planet Sci Lett* 274(1–2):24–33. <https://doi.org/10.1016/j.epsl.2008.06.034>
- Wittig N, Webb M, Pearson DG, Dale CW, Ottley CJ, Hutchison M, Jensen SM, Lugué A (2010) Formation of the North Atlantic Craton: timing and mechanisms constrained from Re–Os isotope and PGE data of peridotite xenoliths from SW Greenland. *Chem Geol* 276(3–4):166–187. <https://doi.org/10.1016/j.chemgeo.2010.06.002>
- Wohlgemuth-Ueberwasser CC, Ballhaus C, Berndt J, Paliulionyte VSN, Meisel T (2007) Synthesis of PGE sulfide standards for laser ablation inductively coupled plasma mass spectrometry (LA-ICP-MS). *Contrib Mineral Petrol* 154:607–617. <https://doi.org/10.1007/s00410-007-0212-x>

**Publisher's Note** Springer Nature remains neutral with regard to jurisdictional claims in published maps and institutional affiliations.